Assessing the timing of deep ocean oxygenation from uranium elemental and isotopic compositions of ophiolites

Joel B. Rodney[a*], Morten B. Andersen[b], Daniel Stubbs[a, c], C. Johan Lissenberg[b], Omar Gianola[d], Matthias Willbold[e], Tim Elliott[a]

[a]Bristol Isotope group, School of Earth Sciences, University of Bristol, Wills Memorial Building, Queen's Road, Bristol, BS8 1RJ, UK

[b]School of Earth & Environmental Sciences, Cardiff University, Park Place, Cardiff, CF10 3AT, UK

[c]National Nuclear Laboratory, Central Laboratory, Sellafield, Cumbria, UK, CA20 1PG

[d]Department of Geosciences, University of Padova, Via G. Gradenigo 6, 35131 Padova, Italy

[e]Georg-August-Universität Göttingen, Geowissenschaftliches Zentrum Göttingen, Abt. Geochemie und Isotopengeologie, Goldschmidtstr. 1, 37077 Göttingen, Germany

*Corresponding author

Email addresses: joel.rodney@bristol.ac.uk (J.B. Rodney), andersenm1@cardiff.ac.uk (M.B. Andersen), dstubbs95@icloud.com (D. Stubbs), lissenbergcj@cardiff.ac.uk (C. J. Lissenberg), omar.gianola@gmail.com (O. Gianola), matthias.willbold@uni-goettingen.de (M. Willbold), tim.elliott@bristol.ac.uk (T. Elliott).

Abstract

The concentration of dissolved oxygen in the deep oceans has varied over Earth History, with the timing of the transition from anoxic to oxic deep oceans debated. Under modern-day, oxic, deep ocean conditions, alteration of the upper sections of mafic oceanic crust with U-rich seawater leads to U enrichment, low Th/U ratios, and heterogeneous $^{238}U/^{235}U$ ratios relative to fresh mid-ocean ridge basalt (MORB). Given the redox sensitivity of U, its uptake into altered mafic oceanic crust (AMOC) is expected to be smaller and less isotopically fractionated when deep oceans were anoxic and thus U-poor. Determining when, in the geological record, the U elemental and isotopic systematics of ancient oceanic crust first resemble modern day AMOC should indicate when deep oceans became oxic. We provide U concentration, Th/U, and U isotopic data on upper-crustal sections of three ophiolites from 750 to 480 Ma, spanning the period inferred for deep ocean oxygenation (~ 850 to 400 Ma). The ophiolites at 480 and 540 Ma have high U contents, low Th/U ratios, and variability in $^{238}U/^{235}U$ ratios like modern-day AMOC, reflecting seawater alteration of oceanic crust under oxygenated seawater conditions. In contrast, the 750 Ma ophiolite does not show the distinctive decreasing Th/U with increasing U concentrations trend of modern AMOC and has fewer samples with $^{238}U/^{235}U$ ratios perturbed from mantle values, reflecting alteration under largely anoxic deep ocean conditions. This is also supported by Fe^{3+}/Fe_T ratios in these samples that are like unaltered modern MORB. Thus, our data suggest oxygenated deep oceans at some time between 750 to 540 Ma, either reflecting a full transition or intermittent deep ocean oxygenation events within an otherwise anoxic deep ocean.

Keywords

Uranium; Seawater alteration; Ophiolites; Altered mafic oceanic crust; Deep ocean oxygenation

1. Introduction

The evolution of oceanic redox state is important for Earth's surface biogeochemical cycles and the evolution of life (e.g., Holland, 1984; Canfield, 1998; Planavsky et al., 2011; Lyons et al., 2014, 2021, 2024 and references therein). Evidence points to the development of an oxic ocean in the late Proterozoic – early Phanerozoic (~ 850 to 400 Ma) in response to the rising abundance of oxygen in the atmosphere (Canfield et al., 2007, 2008; Scott et al., 2008; Sahoo et al., 2012, 2016; Dahl et al., 2014; Lyons et al., 2014; Sperling et al., 2015; Krause et al., 2018, 2022; Stockey et al., 2024). Estimates of the atmospheric O_2 abundance needed to oxygenate the deep oceans are uncertain and range from 15 to 50 % of present atmospheric levels (PAL) (Canfield et al., 2007; Canfield, 2014; Stockey et al., 2024). Estimates of ocean oxygen abundances through this time period are mainly based on elemental and isotopic proxies from sediments on continental shelfs and or slopes (such as C, Fe, U, Mo, Cr, and Zn, e.g., Lyons et al., 2014, 2021, 2024 and references therein).

Differing views have emerged from the various geochemical proxies used to investigate the redox evolution of the atmosphere and oceans from the Proterozoic to the Phanerozoic (e.g., see reviews in Lyons et al., 2014, 2021, 2024; Robbins et al., 2016; Krause et al., 2018, 2022; Mills et al., 2023; Stockey et al., 2024). The mid-late Neoproterozoic (~ 850 to 539 Ma) has long been suggested to be a period of significant change in atmosphere and ocean oxygen content (e.g., Krause et al., 2022; Stockey et al., 2024), with estimates of very low oxygen levels in the time period (<1 % PAL e.g., Planavsky et al., 2014; Sperling et al., 2015; Cole et al., 2016), while other estimates suggest more elevated oxygen levels (4 to ~ 24 % PAL e.g., Zhang et al., 2016; Yang et al., 2017; Canfield et al., 2021). One potential reconciliation using evidence from multiple proxies is that rather than steady conditions, the oceans in this time

117 period likely had considerable variability, with 'brief' (<10 million years) periods of 'ocean
118 oxygenation events', that may have been global or region-specific, against a backdrop of
119 anoxic oceans (e.g., Sahoo et al., 2016; Tostevin and Mills, 2020; Krause et al., 2022). For
120 example U isotopic compositions of sediments point towards brief, punctuated levels of ocean
121 oxygenation in the Proterozoic (e.g., Wei et al., 2021; Chen et al., 2022), potentially as far back
122 as 1000 Ma (e.g., Dang et al., 2022). Recent work from Stockey et al. (2024), using global
123 compilations of U and Mo concentrations in shales and marine biogeochemical signals,
124 narrows the time of deep ocean oxygenation to the Palaeozoic. Stockley et al. (2024) infer an
125 increase in O_2 atmospheric abundance at the Neoproterozoic – Palaeozoic boundary, but not
126 by enough to oxygenate the deep oceans. Large changes in deep ocean conditions from anoxic
127 / suboxic to more oxic conditions are not inferred until the 539 to 400 Ma time period, with
128 potential full deep ocean oxygenation comparable to modern-day at ~ 420 Ma (Stockey et al.,
129 2024). However, many of the proxies used for these estimates may represent local rather than
130 global changes and are largely more representative of the shallower surface level oceans due
131 to being based on sedimentary records. The ongoing debate over the timing of this critical
132 change at Earth's surface environment using existing data, encourages development of new,
133 redox-sensitive, elemental and isotopic tracers.
134
135 More direct proxy estimates of deep ocean redox conditions were obtained by Stolper and
136 Keller (2018) by tracking Fe^{3+}/Fe_T (where Fe_T is total Fe) in extrusive sections of ophiolites,
137 dating back to 3500 Ma. Ophiolites represent the remnants of ancient oceanic crust that were
138 subsequently accreted to the continents, and thus may preserve a record of deep ocean
139 conditions from their interaction with seawater during alteration. Circulation of oxygen-rich
140 seawater through oceanic crust in the deep ocean basins oxidises Fe^{2+} to Fe^{3+}, elevating
141 Fe^{3+}/Fe_T. Values above modern unaltered MORB and back arc basin basalts (Fe^{3+}/Fe_T ~ 0.3)

indicate the interaction of the ophiolite with oxygenated seawater and therefore oxygenated deep oceans. The data of Stolper and Keller (2018) suggest that consistently elevated Fe^{3+}/Fe_T, and so oxygenated ocean bottom waters, are only apparent from the beginning of the Phanerozoic (~ 539 Ma) and possibly not widespread until late Palaeozoic (<420 Ma), in agreement with other works (e.g., Stockey et al., 2024).

Other redox sensitive characteristics of altered mafic oceanic crust (AMOC) may similarly trace deep ocean oxygenation. A notable feature of the uppermost 500 m of modern AMOC is its enrichment in U abundances, by up to an order of magnitude through low temperature interaction with seawater (Hart and Staudigel, 1982; Staudigel et al., 1995; Bach et al., 2003; Kelley et al., 2003). Uranium has two main redox states, reduced and immobile U^{4+} and oxidised and fluid mobile U^{6+} (Langmuir, 1978). After the onset of the first major rise in atmospheric pO_2 across the great oxygenation event (~ 2.3 Ga), there would have been a supply of continent-derived U^{6+} to the oceans due to oxidative continental weathering. However under anoxic marine conditions, the majority of this U would have been reduced and sequestered as immobile U^{4+} complexes into sediments in shallow settings, leading to a low U concentration oceanic reservoir (e.g., Anderson et al., 1989; Klinkhammer and Palmer, 1991; Partin et al., 2013). Only once the oceans became fully oxygenated, would U be appreciably transported to the deep ocean floor as fluid mobile U^{6+}. Lower U removal rates in ocean basins with decreasing area of anoxic seafloor area results in increasing U concentration of seawater. The enrichment of AMOC with seawater U is seen through a general increase in U concentrations and a lowering of the Th/U ratio of AMOC, defining a clear negative trend in U concentration vs. Th/U ratio relative to MORB (Fig. 1a). Thorium acts as a useful comparison to U due to their similar magmatic behaviour, where both are present in the 4+ oxidation state, but different behaviours in the oxidised surface environment, with oxidised U^{6+} being fluid mobile in

contrast to Th, which remains in a non-fluid mobile 4+ oxidation state. Thorium abundances therefore show little change in the oceanic crust during seawater alteration. Associated high U concentration with low Th/U ratio in AMOC, relative to unaltered MORB, is thus indicative of U addition from oxygenated seawater to the oceanic crust (Fig. 1a).

The enrichment and redistribution of U in the oceanic crust during oxygenated seawater alteration is associated with redox sensitive isotopic fractionation that results in AMOC having heterogenous $^{238}U/^{235}U$ compositions. Samples of AMOC have U isotopic compositions that are both heavier (i.e., higher $^{238}U/^{235}U$) and lighter (i.e., lower $^{238}U/^{235}U$) than unaltered MORB, as shown from oceanic drill core sites 801C (Pacific), 417/418 (Atlantic), and 1256D (Pacific) (Andersen et al., 2015; Noordmann et al., 2016; Andersen et al., 2024) (Fig. 1b). In the shallowest portions of AMOC U addition is dominated by sorption of U^{6+} onto secondary mineral surfaces, such as Fe-oxyhydroxides, which favours lighter U isotopes. In deeper regions of AMOC, where conditions become more reducing, seawater transported U^{6+} may undergo partial reduction to U^{4+}, which favours heavier U isotopes, and subsequent incorporation into secondary minerals such as calcite (Andersen et al., 2015, 2024). As the oceanic crust cools and moves off axis, the overlying sediment package thickness increases, so oxidised seawater flow becomes more restricted, conditions become increasingly reducing and the average $^{238}U/^{235}U$ ratio of AMOC becomes isotopically heavier over time due to partial reduction processes becoming dominant (Andersen et al., 2024). Some samples of AMOC with low Th/U ratios and high U concentrations show $^{238}U/^{235}U$ ratios that are similar to modern seawater and MORB, likely representing conditions with quantitative U uptake, with little to no net isotopic fractionation relative to seawater or MORB (Andersen et al., 2024). These contrasting styles of U isotopic fractionation during alteration of mafic oceanic crust on the modern ocean floor are summarised in figure 1b.

A deep ocean dominated by anoxic conditions, would result in a different behaviour of U during oceanic crust alteration. Firstly, seawater would have a much lower capacity for carrying U into the deep oceans and presumably most would be lost in shelf settings. This would strongly limit the magnitude of elemental U enrichment in AMOC. Secondly, the main mechanisms of U incorporation and isotopic fractionation into modern AMOC will operate differently under anoxic conditions; in reducing seawater oxic U^{6+} would not be stable and any U uptake into oceanic crust would occur with more quantitative U^{4+} uptake, resulting in limited isotopic variability in AMOC. Thus, identifying when in geological history AMOC first shows notable U enrichment (with associated low Th/U ratios), and isotopic variability in U should indicate the onset of oxygen-rich deep oceans.

Here, we apply these U elemental and isotopic proxies using measurements of ophiolite samples. We measure the U concentration, Th/U ratio, and natural isotopic variations in U in sample sets from three ophiolites: 750 Ma Gabal Gerf, North Africa (Zimmer et al., 1995), 540 Ma Khantaishir, Mongolia (Gianola et al., 2019), and 480 Ma Annieopsquotch, Canada (Lissenberg et al., 2005) ophiolites, which span the time range suggested for the onset of deep ocean oxygenation (Canfield et al., 2007, 2008; Scott et al., 2008; Sahoo et al., 2012, 2016; Dahl et al., 2014; Lyons et al., 2014; Sperling et al., 2015; Stolper and Keller, 2018; Stockey et al., 2024).

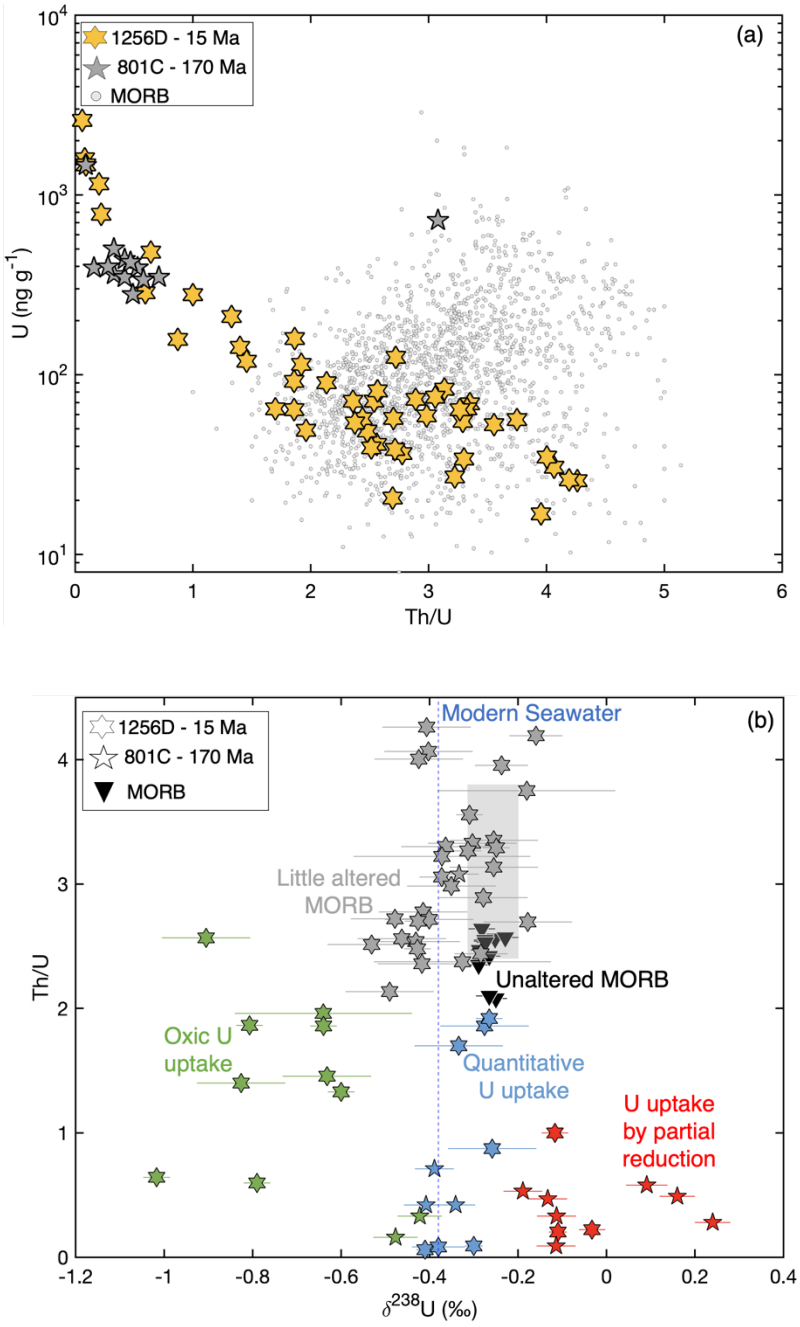

Fig. 1. (a) U concentration vs. Th/U ratio for AMOC samples from the modern ocean floor: ODP holes 801C (~ 170 Ma) (Andersen et al., 2015), 1256D (~ 15 Ma) (Andersen et al., 2024), and a global MORB compilation using a compilation of ICP-MS analyses from Gale et al. (2013). (b) Th/U ratio vs. $\delta^{238}U$ for AMOC samples from the modern ocean floor. Modern seawater composition (Kipp et al. 2022) is shown as a vertical blue dashed line. Grey shaded region represents the average Th/U of normal MORB ± 1 SD using a compilation of ICP-MS

analyses from Gale et al. (2013), and the range in $\delta^{238}U$ for MORB (Andersen et al., 2015). Grey data points are samples that are closest in composition to fresh unaltered MORB (black, inverted triangles). Samples with lower Th/U imply U uptake during alteration but under different redox conditions: green data points are samples that are isotopically light (oxic U^{6+} adsorption), blue data points are samples that are similar to MORB or seawater in $\delta^{238}U$ (quantitative reduction) and indicate quantitative U uptake, red data points are samples that are isotopically heavy (partial reduction of U^{6+} to U^{4+} and uptake). Note that DSDP site 417/418 (Noordmann et al., 2016) also has data for $\delta^{238}U$, however there are no Th/U values, so samples are excluded from this figure. Error bars on $\delta^{238}U$ are 2SE.

2. Geological location and samples

The Annieopsquotch ophiolite, 480 Ma (U/Pb zircon age), (Dunning and Krogh, 1985) in Newfoundland, Canada represents a 5.5 km thick section of magmatic oceanic crust, comprising gabbro, sheeted dykes, and basaltic pillow lavas, with the distribution of hydrous mineralogical assemblages reflecting predominantly ocean floor alteration processes (Lissenberg et al., 2005). It is thought to have formed following subduction initiation in the Iapetus Ocean and have been accreted to the Laurentian continental margin within 10 Myr of formation (Lissenberg et al., 2005). Samples analysed in this work are from the sheeted dykes and extrusive sections.

The Khantaishir ophiolite in Western Mongolia, part of the Central Asian orogenic belt, is divided into the Naran and Taishir massif, both with well-exposed mantle sections, overlain by gabbro, sheeted dyke complexes, and pillow lavas, that have experienced limited greenschist-facies metamorphism that is either ocean floor or accretion related (Gianola et al., 2019). Reported ages for the Khantaishir ophiolite varies, with Sm-Nd ages of 532 ±40 Ma for the Taishir massif and 540 ±12 Ma for the Naran massif (Gianola et al., 2019), while U/Pb dating of plagiogranites suggests ages of 573 ±8 Ma and 566 ±7 Ma (Jian et al., 2014), with an estimated general age range of ~ 550 – 530 Ma (Gianola et al., 2019), we use an average age of 540 Ma in this study. The age of obduction is 514 ±8 Ma (Jian et al., 2014). Samples analysed here are from the crustal section, spanning the gabbro, sheeted dyke complex and extrusive section, composed mostly of basaltic andesite pillow lavas.

The Gabal Gerf ophiolite, in the Southern Eastern Desert of Egypt and Red Sea Hills of Sudan, is the largest mafic-ultramafic ophiolite complex in the Arabian-Nubian shield (Zimmer et al.,

1995). It is comprised of the Gabal Gerf, Gabal Harga Zarga, and Gabal Heiani nappe complexes, containing various rock packages, including serpentinised ultramafic melange, serpentinised or carbonated ultramafics, gabbro, sheeted dykes, basaltic lavas, and pillow lavas which have variably experienced up to greenschist-facies metamorphism (Zimmer et al., 1995). Pooled Sm-Nd ages suggest a mean age of ~ 750 Ma for gabbro crystallisation (Zimmer et al., 1995), with obduction occurring around ~ 715 Ma (Kröner et al., 1992). Samples analysed in this work cover ultramafic cumulates, gabbro, sheeted dyke complexes, and pillow lavas across the three nappes identified.

The Th/Nb ratio places useful constraints on the tectonic settings (Fig. S1a) of formation for each ophiolite (Supplementary Material: Section 1), with inferred spreading centre setting for Gabal Gerf, a suprasubduction zone setting for Khantaishir and spreading centre with slight suprasubduction zone signature for Annieopsquotch. The variability in tectonic setting is not significant for this study, as the U signatures are imparted during seafloor alteration, likely overprinting any primary signature differences. Lavas from volcanic arc settings have slightly lower Th/U ratios, due to U addition from subducting slab dehydration (Fig. S1b), however this is still relatively small compared to the U than can be added during seafloor alteration, which imparts bigger changes to Th/U ratios and U concentrations (Supplementary Material: Section 1). Therefore, we do not treat ophiolite samples from different tectonic settings differently.

316 **3. Methods**

317

318 Details of major and trace element data on the ophiolite samples are reported in Zimmer
319 et al. (1995), Lissenberg et al. (2005), and Gianola et al. (2019). For U isotopic measurement,
320 sample preparation and analysis largely followed Andersen et al. (2015) with some
321 modification, detailed fully in Supplementary Material: Section 2. Uranium isotope analysis
322 was conducted in the University of Bristol Isotope Group laboratories. Approximately 0.5 – 3
323 g of sample powder, spiked with the IRMM3636 ^{236}U – ^{233}U double spike (Richter et al., 2008),
324 aiming for a $^{236}U/^{235}U$ ratio of 5, was dissolved following silicate digestion methods.
325 Purification and U separation used a two-column method, with TRU resin to separate most
326 matrix elements, followed by UTEVA resin to separate remaining matrix and Th from U. Final
327 U aliquots were dissolved in 0.2 M HCl (aiming for U concentrations of 50 – 300 ng g^{-1}) for
328 isotopic analysis. Procedural blanks were <30 pg U, negligible compared to amount of U
329 consumed per measurement (see below). For the measurement of Th and U concentrations
330 (non-isotope dilution), ~ 50 mg of sample powders were dissolved and analysed on a
331 ThermoFinnigan Element2 in the Bristol Isotope Group laboratories following Andersen et al.
332 (2014), measured concentrations of U, Th, and Th/U ratios of reference materials measured on
333 the Element2 are in good agreement with reference values (Supplementary Material: Section
334 2).

335

336 Uranium isotope compositions were measured on a ThermoFinnigan Neptune MC-ICP-MS
337 (serial no. 1002) in low mass resolution ($M/\Delta M$ ~ 2000, 5 to 95 % peak height definition).
338 Samples were introduced to the plasma using a ~ 40 µl min^{-1} micro-concentric PFA nebuliser
339 connected to a Cetac Aridus (1st generation) desolvating system. Ion beams at masses 232
340 (^{232}Th), 233 (^{233}U), 234 (^{234}U), 235 (^{235}U), 236 (^{236}U), and 238 (^{238}U) were measured. Each

sample was preceded and followed by a measurement of the double-spiked standard CRM-145. Individual measurements consisted of 80 cycles of 4.194 s integrations. Samples were measured at varying concentrations, generally between 50 – 300 ng g^{-1}, corresponding to U consumption between ~ 15 – 80 ng per measurement.

Uranium isotope ratios for $^{238}U/^{235}U$ and $^{234}U/^{238}U$ were calculated using the exponential mass fractionation law and reference double spike $^{233}U/^{236}U$ ratio (Richter et al., 2008). Data are reported in δ notation with $\delta^{238}U = [(^{238}U/^{235}U_{Sample} / {}^{238}U/^{235}U_{CRM\text{-}145}) - 1]$ and $\delta^{234}U = [(^{234}U/^{238}U_{Sample} / (^{234}U/^{238}U_{CRM\text{-}145}/ (1–0.0386)) - 1]$. Normalising sample measurements to the average of bracketing CRM-145 analyses removes second order non-exponential mass bias effects from the analyses. Note that $\delta^{234}U$ values are reported relative to secular equilibrium, given the CRM-145 standard has a $\delta^{234}U$ of −38.6 ‰ relative to secular equilibrium (Cheng et al., 2013).

Long term external reproducibility at various measured U intensities has been estimated using aliquots of the well characterised reference material BHVO-2 measured during different analytical sessions. The external reproducibility of $\delta^{238}U$ and $\delta^{234}U$ for BHVO-2 ranges from ±0.09 – 0.03 ‰, 2SD, and ±4 – 0.9 ‰, 2SD, respectively, for measured ^{238}U intensities of 200 – 1000 pA respectively (full details reported in Supplementary Material: Section 2). Uranium isotopic measurements of international reference materials analysed (BHVO-2, BCR-2, BIR, W-2A, and CZ1) agree well with literature values (Supplementary Material: Section 2).

4. Results

All uranium isotopic composition, concentrations, and Th/U ratios made during this study are reported in the Supplementary Material: Section 3 and supplementary table S3. To present a homogeneous dataset, however, we exclude from further discussion, unless stated: 1) samples measured for Th/U ratios, but not U isotopic compositions and 2) amphibolites and peridotite samples from Gabel Gerf, given these lithologies are not represented in the other ophiolites.

Samples from Annieopsquotch (480 Ma) and Khantaishir (540 Ma) show enrichment in U relative to Th above trends defined by unaltered MORB (Fig. 2a). Samples from these ophiolites show a negative trend of U concentration vs. Th/U ratio, with lower Th/U ratios at higher U concentrations. This trend is very similar to that seen in modern sections of AMOC (Fig. 2b). In contrast, Gabel Gerf (750 Ma) samples, which generally have lower Th concentrations (Fig. 2a), have low Th/U ratios in samples that also have low U concentrations (Fig. 2b). Thus, average U concentration of Annieopsquotch and Khantaishir are also higher than the average for Gabel Gerf (61, 103, and 44 ng g^{-1} respectively), which is also the case for just the extrusive samples (66, 96, and 57 ng g^{-1} respectively), although there is considerable scatter in concentrations for all three ophiolites. In figure 2 and subsequent figures, we highlight the samples that show this clear U enrichment relative to modern MORB associated with decreasing Th/U ratios, as observed in AMOC in the current ocean basins (Fig. 1a). Such samples are identified as having a Th/U ratio lower than one standard deviation of average fresh MORB from spreading centres and back arc settings, i.e., Th/U ratio <2.4, using a compilation of ICP-MS analyses from Gale et al. (2013), and U concentrations above 55 ng g^{-1}, the average concentration of depleted MORB from Gale et al. (2013). Nine samples from

391 Khantaishir and five from Annieopsquotch pass these criteria and define a similar array to data
392 from ODP sites 801C and 1256D (Fig. 2a & b).
393
394 Numerous samples from all three ophiolites have $\delta^{238}U$ that overlap with fresh MORB (Fig.
395 2c). Some samples with low Th/U ratios from Annieopsquotch and Khantaishir (and a single
396 sample from Gabel Gerf) have $\delta^{238}U$ lower than fresh MORB, similar to AMOC in the modern
397 ocean basins (Andersen et al., 2015, 2024). However, there are no $\delta^{238}U$ measurements, outside
398 of uncertainty, higher than the field of modern MORB (Fig. 2c).
399
400 Samples from all ophiolites show a large variation in $\delta^{234}U$ with compositions both above and
401 below secular equilibrium, where secular equilibrium is $\delta^{234}U = 0$ (Fig. 3). However, most
402 samples have $\delta^{234}U > 0$ and extend up to ~ +442 ‰, far above modern seawater (145.6 ±0.3 ‰,
403 2SE; Kipp et al., 2022). There are no clear correlations between $\delta^{234}U$ and $\delta^{238}U$ or U
404 concentrations (Fig. 3a & b) or Th/U ratios (Fig. S3), but samples with the highest U
405 concentrations tend to have the least deviation in $\delta^{234}U$ from secular equilibrium (Fig. 3b). This
406 overview excludes the anomalous Khantaishir sample with the highest $\delta^{234}U$ (~ +442 ‰) that
407 also has a high U concentration (~ 183 ng g^{-1}), marked with a cross on figures 2 and 3.
408
409 Figures 2 and 3 distinguish samples by lithology, which provide a coarse index of depth within
410 the ophiolite stratigraphy. Samples with the highest U concentrations and values of $\delta^{238}U$ lower
411 than fresh MORB are predominantly, but not exclusively, from the extrusive sections of
412 ophiolites, i.e., samples near the top of oceanic crust (Fig. S4).
413
414 A full comparison of alteration mineralogy in modern AMOC and our ophiolite samples is
415 beyond the scope of this work. Details can be found elsewhere (e.g., Alt and Honnorez, 1984;

Zimmer et al., 1995; Alt and Teagle, 2003; Lissenberg et al., 2005; Alt et al., 2010; Gianola et al., 2019), but in Supplementary Material: Section 3 we provide some description and representative petrographic images illustrating the typical mineralogy of submarine alteration evident in the samples (Fig. S5).

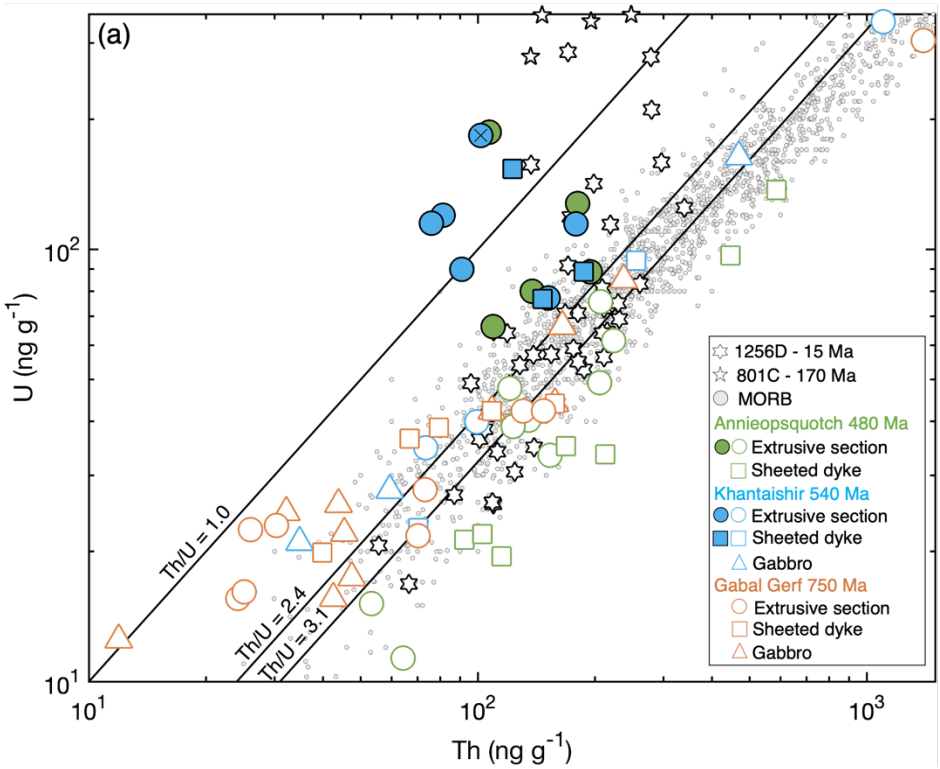
(a)
U (ng g^{-1})
Th (ng g^{-1})
Th/U = 1.0
Th/U = 2.4
Th/U = 3.1
1256D - 15 Ma
801C - 170 Ma
MORB
Annieopsquotch 480 Ma
Extrusive section
Sheeted dyke
Khantaishir 540 Ma
Extrusive section
Sheeted dyke
Gabbro
Gabal Gerf 750 Ma
Extrusive section
Sheeted dyke
Gabbro

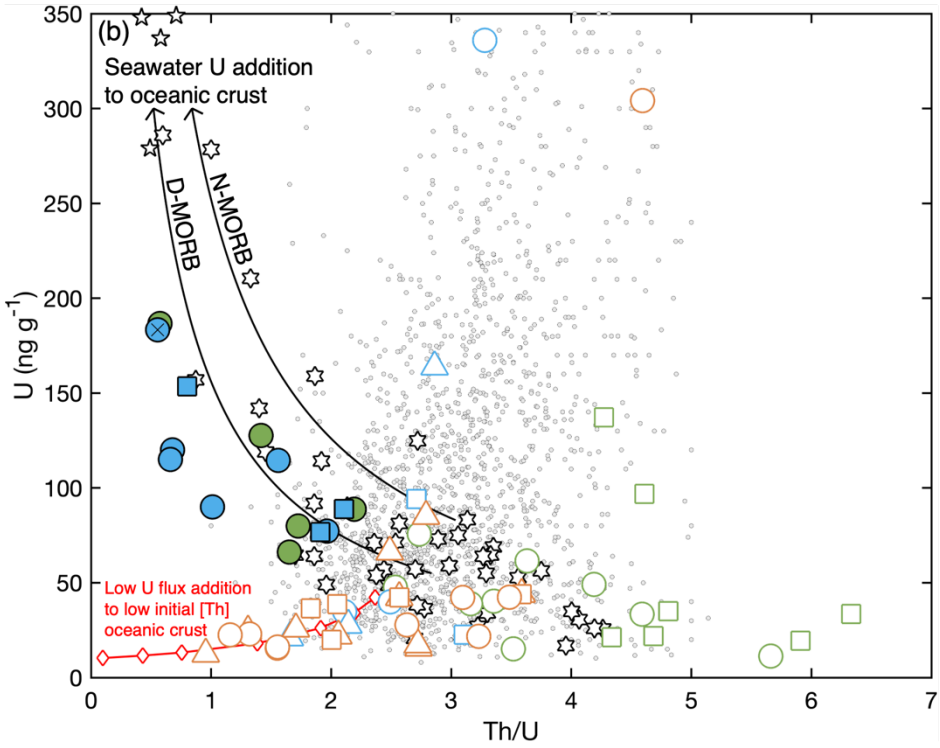
(b)
Seawater U addition
to oceanic crust
D-MORB
N-MORB
Low U flux addition
to low initial [Th]
oceanic crust
U (ng g^{-1})
Th/U

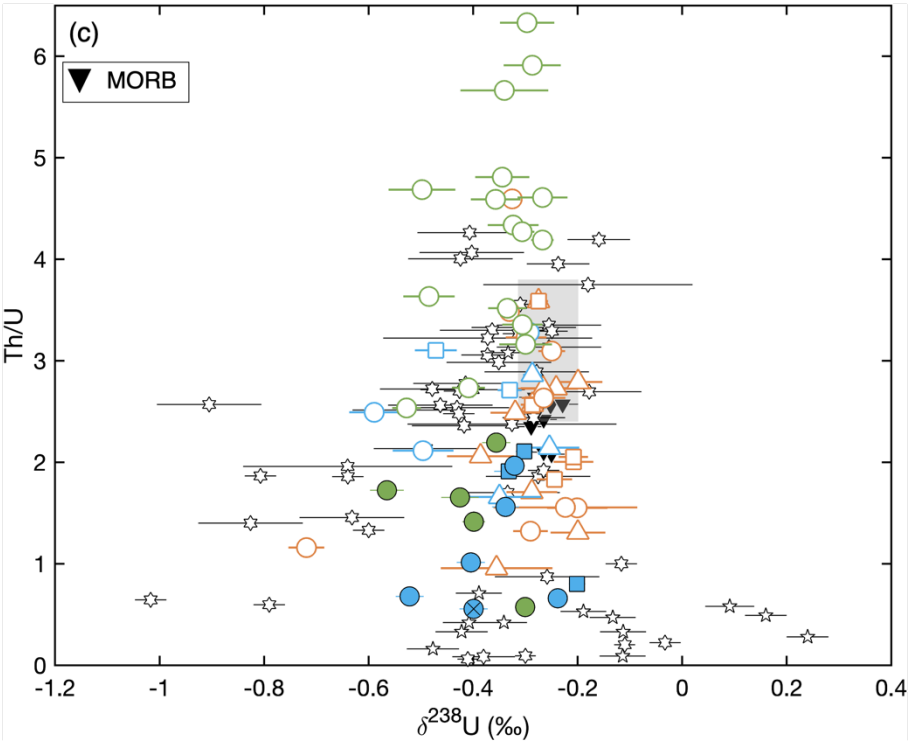

Fig. 2. (a) U concentration vs. Th concentration, (b) U concentration vs. Th/U ratio and (c) Th/U ratio vs. $\delta^{238}U$ for ophiolite samples, modern sections of AMOC (ODP 801C and 1256D), and MORB. Samples from the modern ocean floor are indicated by star (801C) and pentagram (1256D) symbol shapes, and MORB samples as (a, b) small grey circles or (c) inverted triangles. Ophiolite data point shapes are grouped into lithology of samples, circles are samples from the extrusive section, squares are sheeted dykes and triangles are gabbros. Green samples are from Annieopsquotch, blue from Khantaishir, and orange from Gabal Gerf. Ophiolite samples are grouped into two sets, those that show clear negative correlation in U concentration vs. Th/U ratio (filled symbols) and those that do not (hollow symbols), see main text for details. The Khantaishir sample with the highest $\delta^{234}U$ (Fig. 3a) is marked with a cross. In (a) three lines of constant Th/U, 3.1 (average MORB), 2.4, and 1 are shown. Note that the concentrations are on a log scale and have been cut at concentrations of Th 1500 ng g^{-1} and U 350 ng g^{-1}.

In (b) two representative mixing curves (black lines) show the effect of simple U addition to a normal and depleted MORB starting composition from Gale et al. (2013). The red line denotes oceanic crust compositions with variable low initial Th concentrations (white diamonds at 100, 75, 50, 25, 10, 5, and 1 ng g^{-1} Th) and constant Th/U ratio of 3.1 that has been perturbed by a representative equal amount of a low U flux from seawater. Error bars on $\delta^{238}U$ are 2SE.

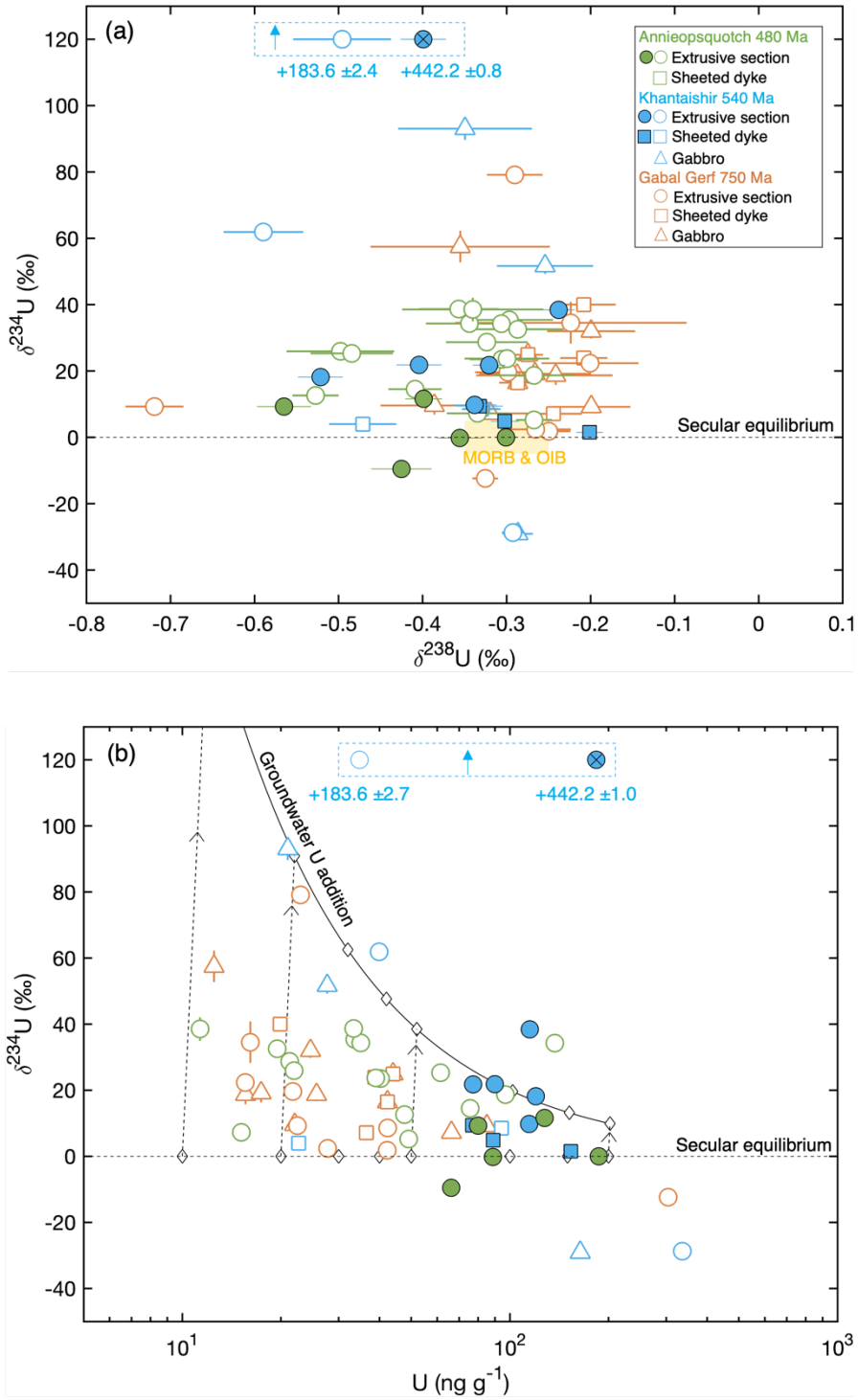

Fig. 3. (a) $\delta^{234}U$ vs. $\delta^{238}U$ and (b) $\delta^{234}U$ vs. U concentration for ophiolite samples. Dashed black line at $\delta^{234}U = 0$ represents secular equilibrium. Ophiolite sample symbol groupings shapes, and colours are the same as in figure 2. Samples from Khantaishir circled in the dashed blue box plot off the scale in $\delta^{234}U$ (Table S3). In (a) the yellow shaded region is the range of $\delta^{234}U$ and $\delta^{238}U$ represented by MORB and ocean island basalt (OIB) samples from Andersen

et al., (2015). In (b) the result of addition of a constant flux of groundwater U (2 ng g^{-1} with $\delta^{234}U$ = 1000 ‰) to samples in secular equilibrium, with a range of initial [U], is shown as the solid black curved line. Vectors of alteration (dashed lines) link specific fresh and altered hypothetical samples (white diamonds) with initial U concentrations (10, 20, 30, 40, 50, 100, 150, and 200 ng g^{-1}). Note that in (b) the U concentration is plotted on a log scale. Error bars are 2SE.

5. Discussion

5.1 Secular equilibrium and sample alteration

The U budgets of ophiolites represent the primary rock inventory with additions from ancient seafloor alteration and possibly more recent sub-aerial exposure. Measurements of $\delta^{234}U$ potentially provide a means to distinguish between the latter two processes. The deviation of samples from secular equilibrium ($\delta^{234}U = 0$) indicates some U loss or gain in the last ~ 2 Myr. Uranium loss during chemical weathering typically leads to ^{234}U deficits ($\delta^{234}U < 0$) through preferential loss of daughter ^{234}U atoms that inevitably sit in damaged recoil sites (Thurber, 1962; Bacon, 1978; MacDougall et al., 1979; Moreira-Nordemann, 1980; Sarin et al., 1990; Chabaux et al., 2003; Gaschnig et al., 2021) resulting in complementary $\delta^{234}U > 0$ of decreasing magnitude in groundwaters, rivers, and the oceans (e.g., Osmond and Cowart, 1976; Dunk et al., 2002; Kipp et al., 2022).

Many samples measured across all three ophiolites have $\delta^{234}U$ values notably higher than secular equilibrium. This implies some recent gain of U by sorption of U from percolating groundwater to secondary minerals (Staudigel et al., 1996; Bach et al., 2001, 2003). The extreme ^{234}U of typical groundwater, $\delta^{234}U$ typically ~ 50 – 1000 ‰ (but can extend to >2000 ‰) (Osmond and Cowart, 1976), means samples can acquire modestly perturbed $\delta^{234}U$ (~ 20 ‰) with only minor elemental U addition. This is illustrated in figure 3b where hypothetical samples with a range of initial U concentrations (white diamonds at secular equilibrium) are perturbed by a fixed addition of groundwater U (2 ng g^{-1} of sample, with a characteristic $\delta^{234}U$ value of 1000 ‰) to all hypothetical samples. This yields the black curve (perturbed hypothetical samples shown as white diamonds along this curve), which are shifted imperceptibly along the x-axis (i.e., minor total U addition) but reproduce much of the

586 variability seen in $\delta^{234}U$, including the tendency for samples with lower U concentration to
587 have higher $\delta^{234}U$. For samples with U concentrations over 20 ng g^{-1} this flux would account
588 for <10 % of the U content of samples, and so a small shift in U concentrations and Th/U ratios
589 but can account for most of the variation in $\delta^{234}U$.
590
591 This is further highlighted by modelling the change in Th/U ratios (Fig. S6a) and $\delta^{238}U$ (Fig.
592 S6b & c) from recent groundwater addition with $\delta^{234}U$ = 1000 ‰, following the approach in
593 Andersen et al. (2024). To account for unknown $\delta^{238}U$ compositions of groundwater we model
594 two scenarios and use the lowest and highest $\delta^{238}U$ compositions in each ophiolite for the
595 groundwater composition. We assume starting $\delta^{234}U$ compositions of 0 ‰ for the rock with no
596 groundwater U addition and apply the model to samples with $\delta^{234}U \geq 0$ ‰ (see Supplementary
597 Material: Section 4 for details). Most samples plot along or within uncertainty of a 1:1 line
598 between corrected compositions for groundwater addition and the measured compositions in
599 Th/U ratio and $\delta^{238}U$ (Fig. S6), bar the sample from Khantaishir with highest $\delta^{234}U$. This simple
600 model highlights that sub-aerial weathering may not have a significant impact on Th/U and
601 $\delta^{238}U$ compositions, even when showing elevated $\delta^{234}U$.
602
603 We have not explored a model of greater complexity, as is done for example in a detailed model
604 by Pavia et al. (2023), that considers a more complete set of serpentinite weathering processes
605 and U isotopic compositions. The simple model curve shown in figure 3b does not account for
606 different amounts of added U, groundwater with different $\delta^{234}U$ or different timing of sample
607 alteration, which all influence individual values of $\delta^{234}U$. The most extreme $\delta^{234}U$, ~ 442 ‰
608 found in a Khantaishir sample (Fig. 3), for example requires an unusually large addition of
609 groundwater U (~ 44 % given groundwater compositions of $\delta^{234}U$ ~ 1000 ‰, table S4). This
610 sample also has the largest shift in Th/U ratio and $\delta^{238}U$ from estimated groundwater addition

(Fig. S6), however the overall affect is again small with corrected compositions still showing evidence of seawater U addition, i.e., low Th/U (measured Th/U 0.6 versus corrected Th/U 1.0). However, an important observation is that samples with high U concentration are not systematically associated with elevated $\delta^{234}U$, indeed the converse is broadly true. This indicates that alteration during recent ophiolite exposure is not the main cause of their U enrichment relative to unaltered MORB.

Furthermore, there is no obvious relationship between $\delta^{234}U$ and $\delta^{238}U$ compositions (Fig. 3a). Much of the range of $\delta^{234}U$ is found in samples with $\delta^{238}U$ within uncertainty of primary magmatic $\delta^{238}U$ (Fig. 3a). This supports the notion developed above that modest perturbation of $\delta^{234}U$ by groundwaters with high $\delta^{234}U$ need not dramatically alter the overall U budget, especially for samples with relatively high U concentrations from submarine alteration acquired before such sub-aerial weathering (Fig. S6). We therefore interpret Th/U ratio and $\delta^{238}U$ in most samples as indicative of compositions resulting from seafloor alteration.

5.2 Comparisons of ophiolites to more recent altered mafic oceanic crust

Our analyses show markedly different patterns of U enrichment in the two younger ophiolites relative to the oldest one. In the former, most samples that have higher U concentrations define a negative trend of U concentration vs. Th/U ratio (Fig. 2b). This pattern mimics that seen in samples of AMOC from the modern seafloor, which is readily explained by the well documented process of U addition during seafloor alteration (e.g., Hart and Staudigel, 1982; Staudigel et al., 1996; Bach et al., 2003; Kelley et al., 2003; Andersen et al., 2015, 2024). Oxic seawater has high concentrations of soluble U^{6+} but very low abundances of insoluble Th^{4+}, so seawater-altered crust acquires elevated U abundances but retains Th little

636 modified from magmatic values. In figure 2b we illustrate this process with lines showing the
637 influence of simple U addition to two examples of unaltered MORB with differing
638 concentrations of U, Th, and Th/U ratios within the range of typical MORB. Some samples
639 from Annieopsquotch extend to high Th/U ratios (>4.5), which may be attributed to some U
640 loss and or remobilisation (Fig. 2a, b), as is seen in some deeper sections of modern AMOC
641 (e.g., Andersen et al., 2024 and references therein).
642
643 Samples from the older, Gabel Gerf ophiolite also show Th/U ratios lower than values seen in
644 unaltered MORB, but this characteristic is evident in samples with the lowest, rather than the
645 highest U content (Fig. 2b). They define a group at low Th and U concentrations, distinct from
646 Khantaishir and Annieopsquotch samples that show signs of high levels of U enrichment
647 similar to modern seafloor samples (Fig. 2a). The small variability in Gabal Gerf likely reflects
648 the addition of small amounts of seawater U to oceanic crust with low initial Th concentration
649 (Fig. 2a & b), which is orders of magnitude smaller than that observed in Khantaishir,
650 Annieopsquotch, and modern AMOC. We illustrate this trend on figure 2b with a red line
651 showing a representative set of oceanic crust compositions with variable low initial Th
652 concentrations (<100 ng g^{-1}) and constant Th/U ratio (3.1) that has been perturbed by a
653 representative equal amount of a low U flux from seawater. This trend can explain the Gabal
654 Gerf samples, as well as some Khantaishir samples that have low Th/U ratios (Fig. 2b) and low
655 Th and U concentrations (Fig. 2a). This is unlike the trends similar to modern AMOC seen in
656 the rest of Khantaishir samples and Annieopsquotch that reflects the addition of large amounts
657 of U to samples with higher Th concentrations (Fig. 2a & b), reflecting oxic deep ocean
658 conditions. There are no Gabel Gerf samples that plot on the highlighted trend of Khantaishir
659 and Annieopsquotch samples to low Th/U ratio at high U concentration (Fig. 2b). The
660 systematics of U and Th trends identified in the Gabal Gerf samples are not characteristic of

661 seawater alteration on the modern ocean floor. They are more readily attributed to minor U
662 addition to seafloor in an anoxic ocean. This suggests that the process of submarine alteration
663 was different at ~ 750 Ma relative to 540 and 480 Ma. We attribute this to changing redox state
664 of the deep oceans during this period and hence seawater U concentration.
665
666 There is a more subtle contrast in the $\delta^{238}U$ between the oldest and more recent ophiolites. All
667 analyses of Gabel Gerf, bar one sample, are within error of modern magmatic $\delta^{238}U$ (Fig. 2c).
668 As argued above, the low Th/U ratio in some Gabel Gerf samples reflect minor seawater U
669 addition to low Th concentration samples. This process appears to result in perturbed $\delta^{238}U$ in
670 only one case, with other samples reflecting non-fractionating bulk addition of minor amounts
671 of U in an anoxic ocean. In contrast, $\delta^{238}U$ in some low Th/U ratio samples from both
672 Khantaishir and Annieopsquotch are significantly lower the unaltered modern MORB (Fig.
673 2c), which we interpret as further evidence of oxic submarine alteration. This is a less definitive
674 signature than the U-Th elemental systematics, as different styles of ^{238}U-^{235}U fractionation are
675 observed with depth in AMOC from the modern ocean floor (Andersen et al., 2015, 2024). In
676 keeping, some of the low Th/U ratio samples from Khantaishir and Annieopsquotch have $\delta^{238}U$
677 within uncertainty of unaltered MORB, likely reflecting quantitative U removal during seafloor
678 alteration.
679
680 It is notable that there are no values of $\delta^{238}U$ in the ophiolite samples higher than unaltered
681 MORB, outside of uncertainty, as can occur through partial reduction of U^{6+} from seawater
682 into the oceanic crust (Fig. 1b). This signature is more diagnostic of older crust on the modern
683 ocean floor (Fig. 4) (Andersen et al., 2015, 2024). Thus, a short timescale between formation
684 and obduction, as might be expected for a marginal basin setting for ophiolitic ocean crust in
685 general and our samples in particular (see section 2), is consistent with the absence of

isotopically heavy values in the Annieopsquotch and Khantaishir samples (Fig. 4). This is also in keeping with the overall muted levels of U enrichment compared to the oldest sections of altered oceanic crust on the modern seafloor (Fig. 4). Admittedly such comparisons are prone to sampling bias and an alternative explanation is that the ophiolite samples we analysed were dominantly collected to study magmatic processes and so the most seawater altered samples (with highest U concentration) may have been systematically avoided.

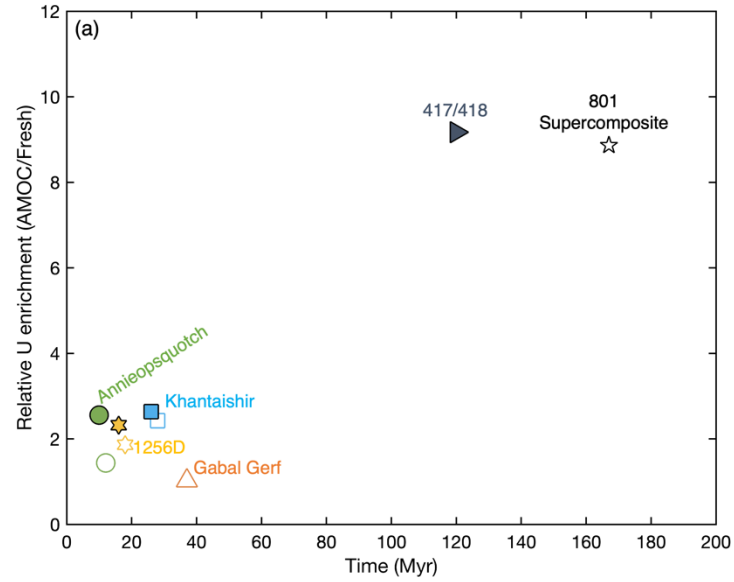

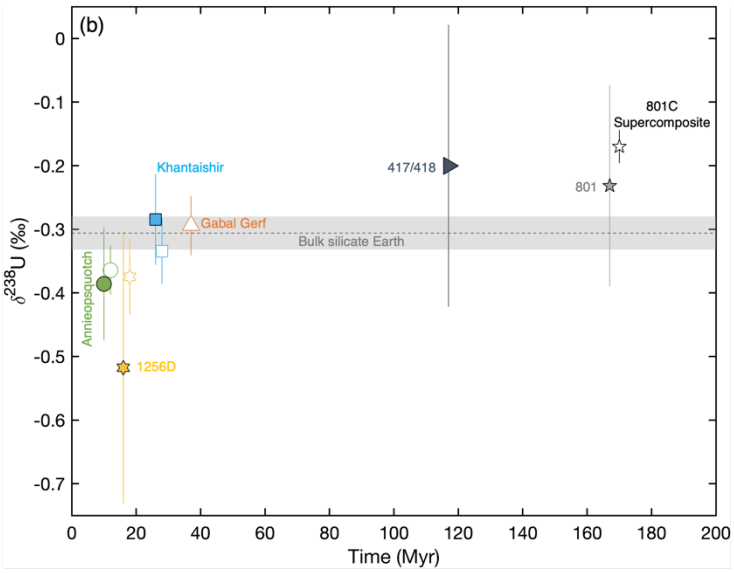

Fig. 4. (a) Average U enrichment and (b) $\delta^{238}U$ vs. time spent on the seafloor for ocean drill site samples and ophiolite samples. Data points from the same location have been artificially separated in time to aid in interpretation. Ocean drill site samples and sources are provided in Supplementary Material: Section 5. Ophiolite time spent on seafloor is calculated as the age of the ophiolite minus the age of obduction. Uranium enrichment calculation is given in Supplementary Material: Section 5 for ocean drill site samples. Ophiolite sample enrichment average is calculated from the average U concentration relative to an average value for fresh MORB from all ocean drill site averages for fresh MORB (~ 43 ng g^{-1}). Uranium enrichment and $\delta^{238}U$ values are calculated using samples with clear signs of U enrichment for Annieopsquotch and Khantaishir (filled symbols), and for all samples (hollow symbols) (excluding peridotite and amphibolite). For ODP 1256D we use data for an average of drill core sections (extrusive, transition zone, and sheeted dykes) excluding the plutonic section (filled symbol) and all samples (hollow symbol). For ODP 801 we use the average of all samples and include the supercomposite measurement of $\delta^{238}U$. The $\delta^{238}U$ composition is calculated as an average weighted by U concentration. Error bars are 2SE.

5.3 Comparison with other recent models of changing ocean anoxia

Given the use of ocean crust alteration recorded in ophiolites in this study, it is valuable to compare our observations to the estimates of deep ocean dissolved O_2 concentrations derived from Fe^{3+}/Fe_T ratios in ophiolites (Stolper and Keller 2018) (Fig. 5a). Stolper and Keller (2018) calculate a gradual increase in the dissolved O_2 concentration of the deep ocean from anoxic conditions (10 ±20 μmol kg^{-1}) in the Neoproterozoic (a period encompassing the Gabel Gerf

736 ophiolite) to values resolvable from zero (30 ±30 μmol kg^{-1}) in the early Palaeozoic (during
737 which Annieopsquotch and Khantaishir were formed and altered), with subsequent continued
738 rise to modern day values of 180 μmol kg^{-1} (Fig. 5a). We note that the Fe^{3+}/Fe_T analyses of the
739 samples used in our study from Gabel Gerf plot amongst the most reduced values in the
740 Neoproterozoic time step of Stolper and Keller (Fig. 5b) and individual samples show no
741 correlation with $\delta^{238}U$ (Fig. S7). Unfortunately, we do not have Fe^{3+}/Fe_T data for our
742 Annieopsquotch or Khantaishir samples.
743
744 The systematic change in style of seawater U addition in between ophiolites of different ages
745 in our study is, at least qualitatively, consistent with the timing of onset of discernible deep
746 ocean oxygenation inferred by Stolper and Keller (2018). However, the Stolper and Keller
747 (2018) model does not show a significant rise in deep oceanic O_2 concentrations until ~ 420
748 Ma, which is younger than the formation and obduction of our youngest ophiolite (480 Ma)
749 which we infer to have experienced alteration in an oxygenated deep ocean. Perfect agreement
750 between the two studies is not expected, as in detail the controls on Fe oxidation and U addition
751 through seawater interaction are different and biased sampling could lead to contrasting
752 inferences from different sample sets. We stress, however, that it is difficult to envisage the
753 extensive addition of U to the mafic oceanic crust, which we observe in 480 and 540 Ma
754 ophiolites, without high U concentration in deep ocean water, which requires an oxygenated
755 deep ocean.
756
757 As mentioned in the introduction, the redox state of the oceans has been more extensively
758 investigated using the concentrations of redox sensitive tracers in marine sediments. The
759 marked rise in U content in some marine sedimentary sections at ~ 600 Ma (e.g., Partin et al.,
760 2013) has been interpreted to reflect the timing of ocean oxygenation, similar to the timing

761 based on arguments from the diversification of life (e.g., Butterfield, 2007; Canfield et al.,
762 2007; Dahl et al., 2010; Lenton et al., 2014; Planavsky et al., 2014). However, a recent study,
763 using a compilation of marine sediment U and Mo concentration data, suggests increasing
764 surface oxygenation across the late Neoproterozoic, early Phanerozoic transition, but no major
765 change in the oxygen content of the deep oceans until ~ 420 – 400 Ma (Stockey et al., 2024).
766 This timing again is significantly later than our inference of deep ocean oxygenation >540 Ma
767 and it is important to reconcile this difference.
768
769 A possible explanation of the different inferred timing of deep ocean oxygenation is that the
770 approaches have a different sensitivity to transient ocean oxygenation events, i.e., brief periods
771 of increased ocean oxygenation against a backdrop of longer scale ocean anoxia. The marine
772 sedimentary data integrates over ~ 10 million years timescales, and as such, may not capture
773 transitory ocean oxygenation events. Although ophiolites also integrate conditions on the deep
774 ocean floor over a similar timescale, a signature of U addition from a short-lived period of
775 oxygenation stands against the unaltered baseline as the signal is not swamped by the averaging
776 with continuing low U concentration input, as in the sedimentary case. Thus, it may be that the
777 U ophiolite proxy can more clearly capture such shorter ocean oxygenation events in an
778 otherwise anoxic deep ocean.
779
780 However, we note that ophiolites provide a direct record of interaction between basaltic rock
781 and deep ocean water, while sedimentary proxies of ocean anoxia trace local conditions on
782 continental shelves and the consequences of these observations for deep ocean conditions
783 requires further biogeochemical modelling. It is interesting to note that the raw sediment U
784 concentration data in the study of Stockey et al. (2024, their supplementary Fig. S2) show a
785 systematic increase the 75th percentile and maximum value in temporally binned samples

younger than ~ 550 Ma. Only with a more sophisticated, statistical learning treatment, to address sample bias, is the rise in sedimentary U content (used to model oxygenation of the deep ocean) delayed until ~ 420 – 400 Ma. Thus, further work is still needed in establishing the timing and style of transition from an anoxic to an oxic deep ocean.

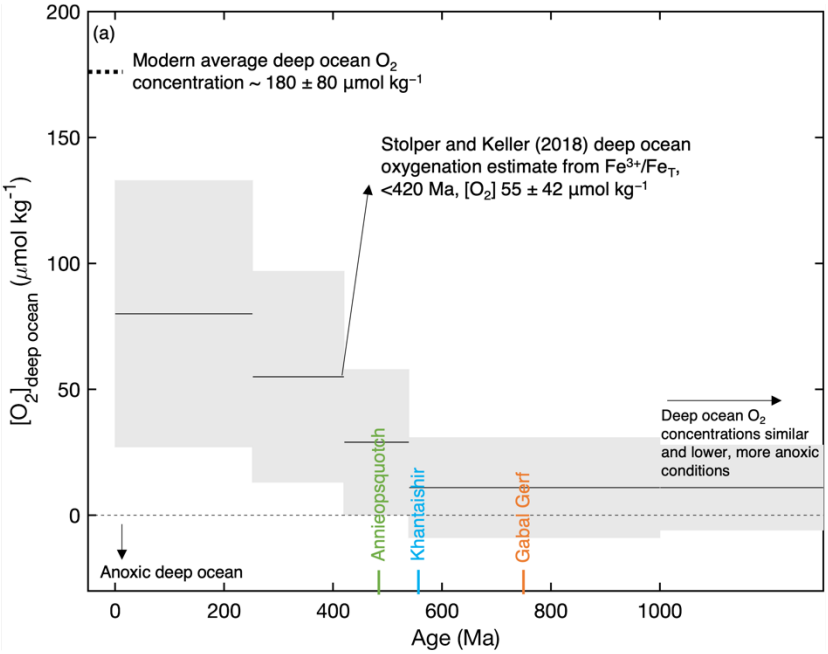

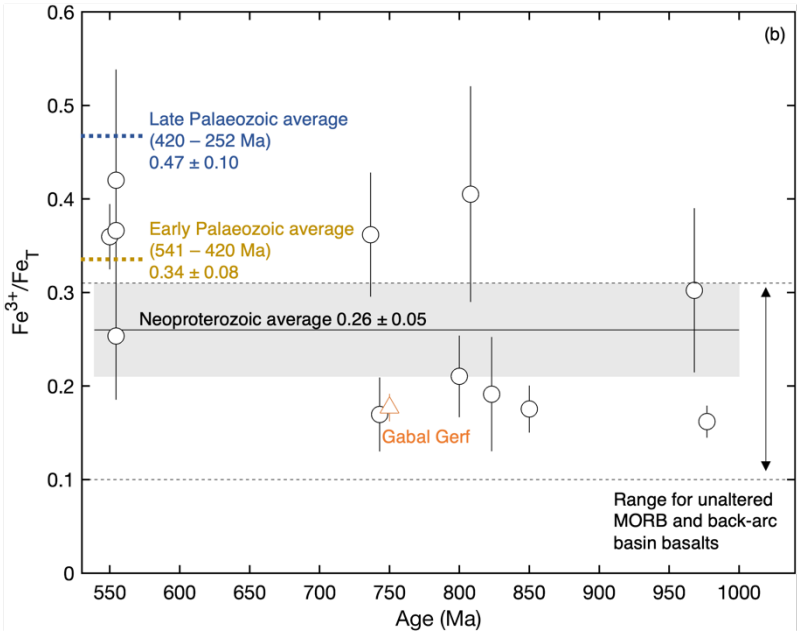

Fig. 5. (a) Modelled deep ocean O_2 concentrations over time from Stolper and Keller (2018) calculated from increases in Fe^{3+}/Fe_T observed in ophiolites relative to unaltered MORB. Thin black lines represent averages and grey shaded region the 2SE. Dotted black line at the top left indicates the O_2 concentration level of modern deep oceans from Sarmiento and Gruber (2006). Figure is based on figure 4a from Stolper and Keller (2018). (b) Iron data for Neoproterozoic ophiolites in the compilation from Stolper and Keller (2018). Data for all Gabal Gerf samples are shown bar the peridotite and amphibolite samples, including samples not measured for $\delta^{238}U$. Error bars are 2SE.

6. Conclusions

Analyses of the Annieopsquotch 480 Ma and Khantaishir 540 Ma ophiolites show samples with low Th/U ratios, high U concentrations and variability in $\delta^{238}U$ that reflect the significant uptake of U into ancient oceanic crust. This implies alteration by oxic, deep ocean water, containing a high concentration of U in its oxidised form, since at least 540 Ma. Such samples also have $\delta^{234}U$ compositions closest to secular equilibrium and are relatively unperturbed by processes following deep sea alteration. Samples from the Gabal Gerf 750 Ma ophiolite do not show these systematics of deep ocean extensive U addition and likely reflect seawater alteration of ocean crust under anoxic conditions. The Th and U elemental and U isotopic compositions of Gabal Gerf are consistent with the Fe^{3+}/Fe_T ratios of the samples, that reflect anoxic alteration conditions. Our data argues for deep ocean oxygenation between 750 – 540 Ma, but it is not clear if the ophiolite data reflect a full transition or intermittent events within a largely anoxic deep ocean. Nonetheless, U abundances and associated Th/U ratios of ophiolites appear to be useful tracers of the oxygenation state of deep ocean water during its alteration of the oceanic crust. The U isotope data provide important supporting information but are less diagnostic given the relatively small isotopic fractionations and ability of different styles of seafloor alteration to cause fractionations in different senses.

Credit authorship contribution statement

Joel B. Rodney: Data curation, formal analysis, investigation, methodology, validation, visualisation, writing – original draft. **Morten B. Andersen:** Supervision, project administration, funding acquisition, conceptualization, methodology, writing – review and editing. **Daniel Stubbs:** Methodology, writing – review and editing. **C. Johan Lissenberg:** Resources, writing – review and editing. **Omar Gianola:** Resources, writing – review and editing. **Matthias Willbold:** Resources, writing – review and editing. **Tim Elliott:** Supervision, project administration, funding acquisition, conceptualization, writing – review and editing.

Declaration of competing interest

The authors declare that they have no known competing financial interests or personal relationships that could have appeared to influence the work reported in this paper.

Data availability

Elemental and isotopic data for ophiolite samples in this study, and a full compilation of ophiolite sample geochemistry data and supplementary data tables S1 to S5 are available through Mendeley data at: https://data.mendeley.com/datasets/fyk72sg4km/3

Acknowledgments

JBR would like to acknowledge Christopher D. Coath and Carolyn Taylor for the upkeep of the mass spectrometry and clean labs. JBR would like to acknowledge Ian Parkinson, Paul Savage, and Lewis Alcott for useful comments that provided improvements to this manuscript. JBR was supported by a NERC GW4 + Doctoral Training Partnership studentship from the Natural Environmental Research Council [NE/S007504/1]. JBR, MBA, and TE acknowledge funding from a NERC grant [NE/T012595/1].

Appendix A. Supplementary Material

Supplementary Material related to this article can be found online at:

908 **References**

909

910 Alt, J. C., and J. Honnorez, 1984, Alteration of the upper oceanic crust, DSDP site 417:
911 mineralogy and chemistry: Contributions to Mineralogy and Petrology, **87**, 149–169.
912 Alt, J. C., and D. A. H. Teagle, 2003, Hydrothermal alteration of upper oceanic crust formed
913 at a fast-spreading ridge: mineral, chemical, and isotopic evidence from ODP Site 801:
914 Chemical Geology, **201**, 191–211.
915 Alt, J. C., C. Laverne, R. M. Coggon, D. A. H. Teagle, N. R. Banerjee, S. Morgan, C. E. Smith-
916 Duque, M. Harris, and L. Galli, 2010, Subsurface structure of a submarine
917 hydrothermal system in ocean crust formed at the East Pacific Rise, ODP/IODP Site
918 1256: Submarine hydrothermal system: Geochemistry, Geophysics, Geosystems, **11**,
919 Q10010.
920 Andersen, M. B., S. Romaniello, D. Vance, S. H. Little, R. Herdman, and T. W. Lyons, 2014,
921 A modern framework for the interpretation of $^{238}U/^{235}U$ in studies of ancient ocean
922 redox: Earth and Planetary Science Letters, **400**, 184–194.
923 Andersen, M. B., T. Elliott, H. Freymuth, K. W. W. Sims, Y. Niu, and K. A. Kelley, 2015, The
924 terrestrial uranium isotope cycle: Nature, **517**, 356–359.
925 Andersen, M. B., J. B. Rodney, H. Freymuth, F. Vils, M. Harris, K. Cooper, D. A. H. Teagle,
926 and T. Elliott, 2024, Time scales and mechanisms of uranium uptake in altered ocean
927 crust; observations from the ~15 million year-old site 1256 in the eastern equatorial
928 Pacific: Geochimica et Cosmochimica Acta, **382**, 142–159.
929 Anderson, R. F., M. Q. Fleisher, and A. P. LeHuray, 1989, Concentration, oxidation state, and
930 particulate flux of uranium in the Black Sea: Geochimica et Cosmochimica Acta, **53**,
931 2215–2224.

Bach, W., B. Peucker-Ehrenbrink, S. R. Hart, and J. S. Blusztajn, 2003, Geochemistry of hydrothermally altered oceanic crust: DSDP/ODP Hole 504B - Implications for seawater-crust exchange budgets and Sr- and Pb-isotopic evolution of the mantle: Hydrothermally altered oceanic crust: Geochemistry, Geophysics, Geosystems, **4**, 8904.

Bach, W., J. C. Alt, Y. Niu, S. E. Humphris, J. Erzinger, and H. J. B. Dick, 2001, The geochemical consequences of late-stage low-grade alteration of lower ocean crust at the SW Indian Ridge: results from ODP Hole 735B (Leg 176): Geochimica et Cosmochimica Acta, **65**, 3267–3287.

Bacon, M. P., 1978, Radioactive disequilibrium in altered mid-oceanic basalts: Earth and Planetary Science Letters, **39**, 250–254.

Butterfield, N. J., 2007, Macroevolution and Macroecology Through Deep Time: Palaeontology, **50**, 41–55.

Canfield, D. E., 1998, A new model for Proterozoic ocean chemistry: Nature, **396**, 450–453.

Canfield, D. E., 2014, 6.8 - Proterozoic Atmospheric Oxygen, *in* H. D. Holland and K. K. Turekian, eds., Treatise on Geochemistry (Second Edition), Elsevier, 197–216.

Canfield, D. E., S. W. Poulton, and G. M. Narbonne, 2007, Late-Neoproterozoic Deep-Ocean Oxygenation and the Rise of Animal Life: Science, **315**, 92–95.

Canfield, D. E., S. W. Poulton, A. H. Knoll, G. M. Narbonne, G. Ross, T. Goldberg, and H. Strauss, 2008, Ferruginous conditions dominated later neoproterozoic deep-water chemistry: Science (New York, N.Y.), **321**, 949–952.

Canfield, D. E., M. A. van Zuilen, S. Nabhan, C. J. Bjerrum, S. Zhang, H. Wang, and X. Wang, 2021, Petrographic carbon in ancient sediments constrains Proterozoic Era atmospheric oxygen levels: Proceedings of the National Academy of Sciences, **118**, e2101544118.

Chabaux, F., J. Riotte, and O. Dequincey, 2003, U-Th-Ra Fractionation During Weathering and River Transport: Reviews in Mineralogy and Geochemistry, **52**, 533–576.

Chen, B., C. Hu, B. J. W. Mills, T. He, M. B. Andersen, X. Chen, P. Liu, M. Lu, R. J. Newton, S. W. Poulton, G. A. Shields, and M. Zhu, 2022, A short-lived oxidation event during the early Ediacaran and delayed oxygenation of the Proterozoic ocean: Earth and Planetary Science Letters, **577**, 117274.

Cheng, H., R. Lawrence Edwards, C.-C. Shen, V. J. Polyak, Y. Asmerom, J. Woodhead, J. Hellstrom, Y. Wang, X. Kong, C. Spötl, X. Wang, and E. Calvin Alexander, 2013, Improvements in ^{230}Th dating, ^{230}Th and ^{234}U half-life values, and U–Th isotopic measurements by multi-collector inductively coupled plasma mass spectrometry: Earth and Planetary Science Letters, **371–372**, 82–91.

Cole, D. B., C. T. Reinhard, X. Wang, B. Gueguen, G. P. Halverson, T. Gibson, M. S. W. Hodgskiss, N. R. McKenzie, T. W. Lyons, and N. J. Planavsky, 2016, A shale-hosted Cr isotope record of low atmospheric oxygen during the Proterozoic: Geology, **44**, 555–558.

Dahl, T. W., R. A. Boyle, D. E. Canfield, J. N. Connelly, B. C. Gill, T. M. Lenton, and M. Bizzarro, 2014, Uranium isotopes distinguish two geochemically distinct stages during the later Cambrian SPICE event: Earth and Planetary Science Letters, **401**, 313–326.

Dahl, T. W., E. U. Hammarlund, A. D. Anbar, D. P. G. Bond, B. C. Gill, G. W. Gordon, A. H. Knoll, A. T. Nielsen, N. H. Schovsbo, and D. E. Canfield, 2010, Devonian rise in atmospheric oxygen correlated to the radiations of terrestrial plants and large predatory fish: Proceedings of the National Academy of Sciences, **107**, 17911–17915.

Dang, D. H., W. Wang, T. M. Gibson, M. Kunzmann, M. B. Andersen, G. P. Halverson, and R. D. Evans, 2022, Authigenic uranium isotopes of late Proterozoic black shale: Chemical Geology, **588**, 120644.

981 Dunk, R. M., R. A. Mills, and W. J. Jenkins, 2002, A reevaluation of the oceanic uranium
982 budget for the Holocene: Chemical Geology, **190**, 45–67.
983 Dunning, G., and T. Krogh, 1985, Geochronology of ophiolites of the Newfoundland
984 Appalachians: Canadian Journal of Earth Sciences, **22**, 1659–1670.
985 Gale, A., C. A. Dalton, C. H. Langmuir, Y. Su, and J.-G. Schilling, 2013, The mean
986 composition of ocean ridge basalts: Geochemistry, Geophysics, Geosystems, **14**, 489–
987 518.
988 Gaschnig, R. M., C. T. Reinhard, N. J. Planavsky, X. Wang, D. Asael, and M. G. Jackson,
989 2021, The impact of primary processes and secondary alteration on the stable isotope
990 composition of ocean island basalts: Chemical Geology, **581**, 120416.
991 Gianola, O., M. W. Schmidt, O. Jagoutz, J. Rickli, O. Bruguier, and O. Sambuu, 2019, The
992 Crust–Mantle Transition of the Khantaishir Arc Ophiolite (Western Mongolia): Journal
993 of Petrology, **60**, 673–700.
994 Hart, S. R., and H. Staudigel, 1982, The control of alkalies and uranium in seawater by ocean
995 crust alteration: Earth and Planetary Science Letters, **58**, 202–212.
996 Holland, H. D., 1984, The Chemical Evolution of the Atmosphere and Oceans: Princeton Univ.
997 Press, Princeton.
998 Jian, P., A. Kröner, B. Jahn, B. Windley, Y. Shi, W. Zhang, F. Zhang, L. Miao, D. Tomurhuu,
999 and D. Liu, 2014, Zircon dating of Neoproterozoic and Cambrian ophiolites in West
1000 Mongolia and implications for the timing of orogenic processes in the central part of
1001 the Central Asian Orogenic Belt: Earth-Science Reviews, **133**.
1002 Kelley, K. A., T. Plank, J. Ludden, and H. Staudigel, 2003, Composition of altered oceanic
1003 crust at ODP Sites 801 and 1149: Geochemistry, Geophysics, Geosystems, **4**, 8910.

1004 Kipp, M. A., H. Li, M. J. Ellwood, S. G. John, R. Middag, J. F. Adkins, and F. L. H. Tissot,
1005 2022, ^{238}U, ^{235}U and ^{234}U in seawater and deep-sea corals: A high-precision reappraisal:
1006 Geochimica et Cosmochimica Acta, **336**, 231–248.
1007 Klinkhammer, G. P., and M. R. Palmer, 1991, Uranium in the oceans: Where it goes and why:
1008 Geochimica et Cosmochimica Acta, **55**, 1799–1806.
1009 Krause, A. J., B. J. W. Mills, A. S. Merdith, T. M. Lenton, and S. W. Poulton, 2022, Extreme
1010 variability in atmospheric oxygen levels in the late Precambrian: Science Advances, **8**,
1011 eabm8191.
1012 Krause, A. J., B. J. W. Mills, S. Zhang, N. J. Planavsky, T. M. Lenton, and S. W. Poulton,
1013 2018, Stepwise oxygenation of the Paleozoic atmosphere: Nature Communications, **9**,
1014 4081.
1015 Kröner, A., W. Todt, I. M. Hussein, M. Mansour, and A. A. Rashwan, 1992, Dating of late
1016 Proterozoic ophiolites in Egypt and the Sudan using the single grain zircon evaporation
1017 technique: Precambrian Research, **59**, 15–32.
1018 Langmuir, D., 1978, Uranium solution-mineral equilibria at low temperatures with applications
1019 to sedimentary ore deposits: Geochimica et Cosmochimica Acta, **42**, 547–569.
1020 Lenton, T. M., R. A. Boyle, S. W. Poulton, G. A. Shields-Zhou, and N. J. Butterfield, 2014,
1021 Co-evolution of eukaryotes and ocean oxygenation in the Neoproterozoic era: Nature
1022 Geoscience, **7**, 257–265.
1023 Lissenberg, C. J., C. R. van Staal, J. H. Bédard, and A. Zagorevski, 2005, Geochemical
1024 constraints on the origin of the Annieopsquotch ophiolite belt, Newfoundland
1025 Appalachians: Geological Society of America Bulletin, **117**, 1413.
1026 Lyons, T. W., C. T. Reinhard, and N. J. Planavsky, 2014, The rise of oxygen in Earth's early
1027 ocean and atmosphere: Nature, **506**, 307–315.

Lyons, T. W., C. W. Diamond, N. J. Planavsky, C. T. Reinhard, and C. Li, 2021, Oxygenation, Life, and the Planetary System during Earth's Middle History: An Overview: Astrobiology, **21**, 906–923.

Lyons, T. W., C. J. Tino, G. P. Fournier, R. E. Anderson, W. D. Leavitt, K. O. Konhauser, and E. E. Stüeken, 2024, Co-evolution of early Earth environments and microbial life: Nature Reviews Microbiology, **22**, 572–586.

MacDougall, J. D., R. C. Finkel, J. Carlson, and S. Krishnaswami, 1979, Isotopic evidence for uranium exchange during low-temperature alteration of oceanic basalt: Earth and Planetary Science Letters, **42**, 27–34.

Mills, B. J. W., A. J. Krause, I. Jarvis, and B. D. Cramer, 2023, Evolution of Atmospheric O2 Through the Phanerozoic, Revisited: Annual Review of Earth and Planetary Sciences, **51**, 253–276.

Moreira-Nordemann, L. M., 1980, Use of $^{234}U/^{238}U$ disequilibrium in measuring chemical weathering rate of rocks: Geochimica et Cosmochimica Acta, **44**, 103–108.

Noordmann, J., S. Weyer, R. B. Georg, S. Jöns, and M. Sharma, 2016, $^{(238)}U/^{(235)}U$ isotope ratios of crustal material, rivers and products of hydrothermal alteration: new insights on the oceanic U isotope mass balance: Isotopes in Environmental and Health Studies, **52**, 141–163.

Osmond, J. K., and J. B. Cowart, 1976, The theory and uses of natural uranium isotopic variations in hydrology: Atomic Energy Review, **14**, 621–679.

Partin, C. A., A. Bekker, N. J. Planavsky, C. T. Scott, B. C. Gill, C. Li, V. Podkovyrov, A. Maslov, K. O. Konhauser, S. V. Lalonde, G. D. Love, S. W. Poulton, and T. W. Lyons, 2013, Large-scale fluctuations in Precambrian atmospheric and oceanic oxygen levels from the record of U in shales: Earth and Planetary Science Letters, **369–370**, 284–293.

Pavia, F. J., E. H. G. Cooperdock, J. C. de Obeso, K. W. W. Sims, F. L. H. Tissot, and F. Klein, 2023, Uranium isotopes as tracers of serpentinite weathering: Earth and Planetary Science Letters, **623**, 118434.

Planavsky, N. J., C. T. Reinhard, X. Wang, D. Thomson, P. McGoldrick, R. H. Rainbird, T. Johnson, W. W. Fischer, and T. W. Lyons, 2014, Low Mid-Proterozoic atmospheric oxygen levels and the delayed rise of animals: Science, **346**, 635–638.

Planavsky, N. J., P. McGoldrick, C. T. Scott, C. Li, C. T. Reinhard, A. E. Kelly, X. Chu, A. Bekker, G. D. Love, and T. W. Lyons, 2011, Widespread iron-rich conditions in the mid-Proterozoic ocean: Nature, **477**, 448–451.

Richter, S., A. Alonso-Munoz, R. Eykens, U. Jacobsson, H. Kuehn, A. Verbruggen, Y. Aregbe, R. Wellum, and E. Keegan, 2008, The isotopic composition of natural uranium samples - Measurements using the new n(^{233}U)/n(^{236}U) double spike IRMM-3636: International Journal of Mass Spectrometry, **269**, 145–148.

Robbins, L. J., S. V. Lalonde, N. J. Planavsky, C. A. Partin, C. T. Reinhard, B. Kendall, C. Scott, D. S. Hardisty, B. C. Gill, D. S. Alessi, C. L. Dupont, M. A. Saito, S. A. Crowe, S. W. Poulton, A. Bekker, T. W. Lyons, and K. O. Konhauser, 2016, Trace elements at the intersection of marine biological and geochemical evolution: Earth-Science Reviews, **163**, 323–348.

Sahoo, S. K., N. J. Planavsky, B. Kendall, X. Wang, X. Shi, C. Scott, A. D. Anbar, T. W. Lyons, and G. Jiang, 2012, Ocean oxygenation in the wake of the Marinoan glaciation: Nature, **489**, 546–549.

Sahoo, S. K., N. J. Planavsky, G. Jiang, B. Kendall, J. D. Owens, X. Wang, X. Shi, A. D. Anbar, and T. W. Lyons, 2016, Oceanic oxygenation events in the anoxic Ediacaran ocean: Geobiology, **14**, 457–468.

1076 Sarin, M. M., S. Krishnaswami, B. L. K. somayajulu, and W. S. Moore, 1990, Chemistry of
1077 uranium, thorium, and radium isotopes in the Ganga-Brahmaputra river system:
1078 Weathering processes and fluxes to the Bay of Bengal: Geochimica et Cosmochimica
1079 Acta, **54**, 1387–1396.
1080 Sarmiento, J. L., and N. Gruber, 2006, Ocean Biogeochemical Dynamics: Princeton University
1081 Press.
1082 Scott, C., T. W. Lyons, A. Bekker, Y. Shen, S. W. Poulton, X. Chu, and A. D. Anbar, 2008,
1083 Tracing the stepwise oxygenation of the Proterozoic ocean: Nature, **452**, 456–459.
1084 Sperling, E. A., C. J. Wolock, A. S. Morgan, B. C. Gill, M. Kunzmann, G. P. Halverson, F. A.
1085 Macdonald, A. H. Knoll, and D. T. Johnston, 2015, Statistical analysis of iron
1086 geochemical data suggests limited late Proterozoic oxygenation: Nature, **523**, 451–454.
1087 Staudigel, H., T. Plank, B. White, and H.-U. Schmincke, 1996, Geochemical Fluxes During
1088 Seafloor Alteration of the Basaltic Upper Oceanic Crust: DSDP Sites 417 and 418, *in*
1089 Subduction, eds: G.E Bebout, D.W. Scholl, S.H. Kirby and J.P. Platt), Geophysical
1090 Monograph Series, 96, American Geophysical Union (AGU), 19–38.
1091 Staudigel, H., G. R. Davies, S. R. Hart, K. M. Marchant, and Brian. M. Smith, 1995, Large
1092 scale isotopic Sr, Nd and O isotopic anatomy of altered oceanic crust: DSDP/ODP
1093 sites417/418: Earth and Planetary Science Letters, **130**, 169–185.
1094 Stockey, R. G., D. B. Cole, U. C. Farrell, H. Agić, T. H. Boag, J. J. Brocks, D. E. Canfield, M.
1095 Cheng, P. W. Crockford, H. Cui, T. W. Dahl, L. Del Mouro, K. Dewing, S. Q. Dornbos,
1096 J. F. Emmings, R. R. Gaines, T. M. Gibson, B. C. Gill, G. J. Gilleaudeau, K. Goldberg,
1097 R. Guilbaud, G. Halverson, E. U. Hammarlund, K. Hantsoo, M. A. Henderson, C. M.
1098 Henderson, M. S. W. Hodgskiss, A. J. M. Jarrett, D. T. Johnston, P. Kabanov, J.
1099 Kimmig, A. H. Knoll, M. Kunzmann, M. A. LeRoy, C. Li, D. K. Loydell, F. A.
1100 Macdonald, J. M. Magnall, N. T. Mills, L. M. Och, B. O'Connell, A. Pagès, S. E. Peters,

S. M. Porter, S. W. Poulton, S. R. Ritzer, A. D. Rooney, S. Schoepfer, E. F. Smith, J. V. Strauss, G. J. Uhlein, T. White, R. A. Wood, C. R. Woltz, I. Yurchenko, N. J. Planavsky, and E. A. Sperling, 2024, Sustained increases in atmospheric oxygen and marine productivity in the Neoproterozoic and Palaeozoic eras: Nature Geoscience, **17**, 667–674.

Stolper, D. A., and C. B. Keller, 2018, A record of deep-ocean dissolved O_2 from the oxidation state of iron in submarine basalts: Nature, **553**, 323–327.

Thurber, D. L., 1962, Anomalous U^{234} U^{238} in nature: Journal of Geophysical Research, **67,** 11, 4518-4520.

Tostevin, R., and B. J. W. Mills, 2020, Reconciling proxy records and models of Earth's oxygenation during the Neoproterozoic and Palaeozoic: Interface Focus, **10**, 20190137.

Wei, G.-Y., N. J. Planavsky, T. He, F. Zhang, R. G. Stockey, D. B. Cole, Y.-B. Lin, and H.-F. Ling, 2021, Global marine redox evolution from the late Neoproterozoic to the early Paleozoic constrained by the integration of Mo and U isotope records: Earth-Science Reviews, **214**, 103506.

Yang, S., B. Kendall, X. Lu, F. Zhang, and W. Zheng, 2017, Uranium isotope compositions of mid-Proterozoic black shales: Evidence for an episode of increased ocean oxygenation at 1.36 Ga and evaluation of the effect of post-depositional hydrothermal fluid flow: Precambrian Research, **298**, 187–201.

Zhang, S., X. Wang, H. Wang, C. J. Bjerrum, E. U. Hammarlund, M. M. Costa, J. N. Connelly, B. Zhang, J. Su, and D. E. Canfield, 2016, Sufficient oxygen for animal respiration 1,400 million years ago: Proceedings of the National Academy of Sciences, **113**, 1731–1736.

Zimmer, M., A. Kröner, K. P. Jochum, T. Reischmann, and W. Todt, 1995, The Gabal Gerf complex: A precambrian N-MORB ophiolite in the Nubian Shield, NE Africa: Chemical Geology, **123**, 29–51.

Assessing the timing of deep ocean oxygenation from uranium elemental and isotopic compositions of ophiolites

Joel B. Rodney[a*], Morten B. Andersen[b], Daniel Stubbs[a, c], C. Johan Lissenberg[b], Omar Gianola[d], Matthias Willbold[e], Tim Elliott[a]

[a]Bristol Isotope group, School of Earth Sciences, University of Bristol, Wills Memorial Building, Queen's Road, Bristol, BS8 1RJ, UK

[b]School of Earth & Environmental Sciences, Cardiff University, Park Place, Cardiff, CF10 3AT, UK

[c]National Nuclear Laboratory, Central Laboratory, Sellafield, Cumbria, UK, CA20 1PG

[d]Department of Geosciences, University of Padova, Via G. Gradenigo 6, 35131 Padova, Italy

[e]Georg-August-Universität Göttingen, Geowissenschaftliches Zentrum Göttingen, Abt. Geochemie und Isotopengeologie, Goldschmidtstr. 1, 37077 Göttingen, Germany

*Corresponding author

Email addresses: joel.rodney@bristol.ac.uk (J.B. Rodney), andersenm1@cardiff.ac.uk (M.B. Andersen), dstubbs95@icloud.com (D. Stubbs), lissenbergcj@cardiff.ac.uk (C. J. Lissenberg), omar.gianola@gmail.com (O. Gianola), matthias.willbold@uni-goettingen.de (M. Willbold), tim.elliott@bristol.ac.uk (T. Elliott).

Supplementary Information

Section 1: Relative Thorium to Niobium and tectonic setting differences of mantle basalts and ophiolite samples

Section 2: Full detailed method description for U isotopic analysis

Section 3: Ophiolite data and data tables

Section 4: Recent U addition from a groundwater source modelling

Section 5: Uranium enrichment and isotopic variation in AMOC calculations

Section 6: Iron systematics

Section 1:

Relative Thorium to Niobium and tectonic setting differences of mantle basalts and ophiolite samples

Relative Th to Nb concentrations can differentiate tectonic settings of ophiolite formation, with suprasubduction zone settings showing elevated incompatible element signatures similar to arc lavas, e.g., elevated Th relative to Nb (Dilek and Furnes, 2011) (Fig. S1a). Gabal Gerf samples mostly overlap with MORB from mid-ocean ridge spreading centres (Zimmer et al., 1995). Khantaishir samples overlap with volcanic arc samples, indicating an enriched source in a suprasubduction zone setting (Gianola et al., 2019). Annieopsquotch samples fall in-between the two and can be identified as MORB with a slight suprasubduction zone signature (Lissenberg et al., 2005) (Fig. S1a). The variability in tectonic setting is not significant for this study, as the U signatures being compared are imparted during secondary alteration, likely overprinting any primary signature differences. One potential issue relates to Th/U ratios and how much these differ between fresh magmas in different tectonic settings. A key indicator of U enrichment during alteration is a lowering of Th/U. If basalts from different tectonic settings have different starting Th/U ratios, this can make identification of alteration using Th/U ratios challenging. However, no systematic difference in the Th/U ratio of basalt formed in spreading centres and back arcs is seen, and only a small difference with volcanic arcs that extend to lower Th/U, presumably due to some U addition from slab dehydration (Fig. S1b). Even then, volcanic arc lavas have only slightly lower average Th/U (~ 2.3, fig. S1b), which is not as low as the majority of samples that show high U enrichments in modern AMOC (Fig. S1b), with for example the average Th/U of extrusive samples from ODP 1256D being ~ 1.9 (Andersen et al., 2024). Therefore, we see no reason to treat ophiolite samples from different tectonic settings differently, as the main indicators we are looking for from seawater alteration overprint any primary differences from different tectonic settings.

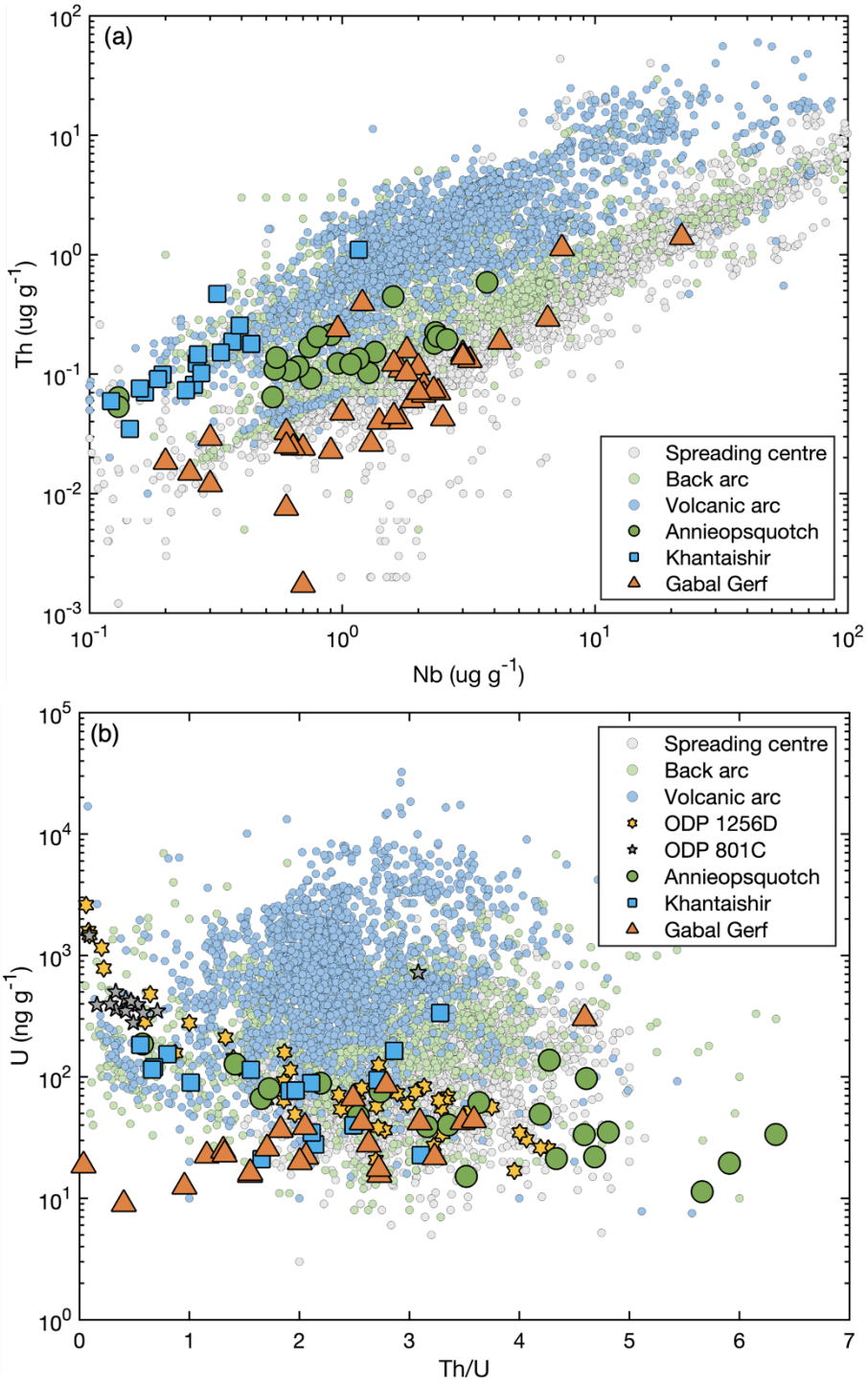

Fig. S1. (a) Th vs. Nb concentration and (b) U concentration vs. Th/U ratio for ophiolite samples and analyses of whole rock and glass samples from spreading centres, back arcs, and volcanic arcs, and ODP 1256D and 801C. Literature data for back arc and volcanic arc samples downloaded from PetDB on 23/09/2021 using data for whole rock and glass samples, data for spreading centres is from the N-MORB dataset from Gale et al. (2013). Data for ODP 1256D and 801C are from Andersen et al. (2024) and Andersen et al. (2015) respectively. Measurements for ophiolite samples are from Element2 ICP-MS measurements and isotope dilution measurements (U), and Nb data from - Annieopsquotch - Lissenberg et al. (2005), Khantaishir - Gianola et al. (2019), and Gabal Gerf - Zimmer et al. (1995).

Section 2:

Full detailed method description for U isotopic analysis

Rock powders and associated major and trace element data were obtained for ophiolite samples, with detailed methods referenced to Zimmer et al. (1995), Lissenberg et al. (2005) and Gianola et al. (2019). For the U isotopic measurements, sample preparation and analysis largely followed Andersen et al. (2015) with some modification. Uranium isotope analysis was conducted in the University of Bristol isotope geochemistry laboratories. Approximately 0.5 − 3 g (variable to obtain a given U amount for measurement) of sample powder was digested in pre-cleaned Teflon PFA beakers. one gramme of sample powder was digested in ~ 24 ml of acid (or appropriately scaled volume for different mass samples) using a mixture of 5:1 15.6 M HNO_3 and Romil UpA 28.1 M HF and placed on a tabletop hotplate at 120 °C for at least 48 hours. Samples were then evaporated to dryness and re-dissolved twice in 6 M HCl to remove fluoride precipitates and achieve full sample dissolution. When more than 1 g of sample was required due to low U concentrations, multiple PFA beakers were used to achieve dissolution of separate splits of samples, before partial evaporation and combination into one beaker. For samples that contained large amounts of refractory minerals such as spinel, they were centrifuged, and the supernatant decanted off solid residues. Solid residues were placed in PARR bombs with a mixture of Aqua regia + trace HF at 200 °C for 168 hours. Once full dissolution was achieved samples were recombined and prepared for ion-exchange columns. The double spike tracer, IRMM3636 ^{236}U – ^{233}U, 50:50 (Richter et al., 2008), was added to samples prior to dissolution in most instances, except where multiple aliquots were digested separately and later combined, in this case, the spike was added after recombination of the sample. The double spike was added to samples according to their U concentrations aiming for a $^{236}U/^{235}U$ ratio of 5. For measurement of Th and U concentrations (non-isotope dilution), small amounts of samples (~ 50 mg) were dissolved and measured on an Element2 at the University of Bristol following Andersen et al. (2014).

Samples were loaded in 40 ml of 1.5 M HNO_3 onto 1 ml of TRU resin (100 – 150 mesh) in commercially available Bio-Rad Poly-Prep columns. Matrix was eluted in 30 ml of 1.5 M HNO_3, before U was collected in 11 ml of 0.3 M HF – 0.1 M HCl. Where over 1 g of sample was dissolved the sample was split over multiple columns, with a maximum of 1 g of digested sample being processed using a single column. When samples were divided, the collected aliquots were re-combined post-chemistry. Samples were dried and fluxed in a 1 ml 50:50 15.6

M HNO_3: 30 % Romil SpA H_2O_2 mixture to eliminate any organic material that may have leached off resin into samples. Samples were loaded in 5 ml 3 M HNO_3 onto 0.5 ml of UTEVA resin (100 – 150 mesh), for Th and U separation, with 10 ml of 3 M HNO_3 washed through to elute any residual matrix, before washing through 15 ml of 5 M HCl to elute Th, before collection of U in 6 ml of 0.3 M HF – 0.1 M HCl. Again, any potential organic material was eliminated from samples. Final U collections were then dried and re-dissolved in a requisite amount of 0.2 M HCl (aiming for U concentration of 50 – 300 ng g^{-1}) for isotopic analysis. This procedure achieved efficient removal of Th and Th/U ratios during isotopic analysis were typically <0.005. For samples VL01J188, VL01J191, VL01J 195, VL01J201, and VL01J205b a prior UTEVA chemistry method using 3 M HCl (Andersen et al., 2015) was used for Th separation, this resulted in less efficient Th removal and Th/U ratios ~ 0.1 in measured sample aliquots. A correction for the high mass plus hydride tailing of $^{232}Th^{1}H^{+}$ on the mass 233 and 234 ion beams was applied in these cases.

Uranium isotope compositions were measured on a ThermoFinnigan Neptune MC-ICP-MS (serial no. 1002) at the Bristol Isotope group in low mass resolution ($M/\Delta M$ ~ 2000, 5 to 95 % peak height definition), using the setup detailed in Andersen et al. (2015). Samples were introduced to the plasma using a ~ 40 µl min^{-1} micro-concentric PFA nebuliser connected to a Cetac Aridus (1^{st} generation) desolvating system. A standard sample cone plus X-skimmer cone set up was used, with a jet sample cone plus X-skimmer cone method also used for low U concentration samples, which gives enhanced sensitivity allowing for improved precision, results obtained via both set ups are indistinguishable (Andersen et al., 2015). Masses 232 (^{232}Th), 233 (^{233}U), 234 (^{234}U), 236 (^{236}U), and 238 (^{238}U) were collected in faraday cups, with most cups connected to feedback amplifiers with 10^{11} Ω resistors, apart from 234 which was connected to a 10^{12} or 10^{13} Ω resistor (after they became commercially available) and 238 which was connected to a 10^{10} Ω resistor. Each sample was preceded and followed by a measurement of the double-spiked (with a double spike proportion similar to samples) standard CRM-145. Individual measurements consisted of 80 cycles each, with 4.194 s integrations, samples were measured at varying concentrations, generally between 50 − 300 ng g^{-1}, correlating to U consumption between ~ 15 − 80 ng per measurement. Procedural blanks were <30 pg U, an insignificant amount compared to amount of U consumed per measurement. Ion beam intensities were corrected for low mass tailings of ion beams and high mass plus hydride tailings of ion beams following Andersen et al. (2015).

The measured double spike isotope ratio of $^{233}U/^{236}U$ was used with the exponential mass fractionation law to correct for mass fractionation of isotope ratios in samples and bracketing standards (Richter et al., 2008). Ratios were also corrected for the minute ^{238}U, ^{235}U and ^{234}U contributions from the IRM-3636 double spike (Condon et al., 2010; Hiess et al., 2012). Uranium isotope ratios for $^{238}U/^{235}U$ and $^{234}U/^{238}U$ are reported in δ notation with $\delta^{238}U = [(^{238}U/^{235}U_{Sample} / {}^{238}U/^{235}U_{CRM\text{-}145}) - 1]$ and $\delta^{234}U = [(^{234}U/^{238}U_{Sample} / (^{234}U/^{238}U_{CRM\text{-}145}/ (1-0.0386)) - 1]$. By normalising sample measurements to the average of bracketing CRM-145 analyses, this removes second order non-exponential mass bias effects from the analyses. Note that $\delta^{234}U$ values are reported relative to secular equilibrium, where the CRM-145 standard has a $\delta^{234}U$ of −38.6 ‰ relative to secular equilibrium (Cheng et al., 2013).

Long term external reproducibility at various measured U intensities has been estimated using aliquots of the well characterised reference material BHVO-2 measured during different analytical sessions. The external reproducibility of $\delta^{238}U$ and $\delta^{234}U$ for BHVO-2 at various intensities (e.g., ^{238}U = 200 − 1000 pA) ranges from ±0.09 − 0.03 ‰, 2SD, and ±4 − 0.9 ‰, 2SD, respectively. The external reproducibility of unknown samples has been determined from the long-term external reproducibility of BHVO-2 measured at various intensities. As samples were measured at varying intensities (~ ^{238}U = 200 − 1000 pA) depending on the U concentration, BHVO-2 was also ran at varying intensities. Repeat measurements of BHVO-2 were then used to estimate the uncertainty of measurements at a given intensity using the 2SD of BHVO-2 measurements in ranges of intensities. A power law was fit to the data for $\delta^{238}U$ and $\delta^{234}U$ at the different intensities and used to approximate errors for unknown samples. This relationship was then used for samples of a given intensity, from which an approximate 2SD could be calculated and an external 2SE calculated based on the number of repeats (Fig. S2).

Uranium isotopic measurements of international reference materials analysed (BHVO-2, BCR-2, BIR, uraninite, CZ1) agree well with values reported by other studies (Table S1). We also report data for a set of in-house reference materials (LP45d, GUG11, and IT3a) that agree well with previous data, and report data on international reference material W-2A ($\delta^{238}U$ −0.289 ‰ ±0.04, 2SD, and $\delta^{234}U$ 2.1 ‰ ±1.4, 2SD, N = 35), such that it can be used for comparison in further studies. Full list of reference material data is provided in Table S1, as well as Element2 ICP-MS reference material measurements in Table S2.

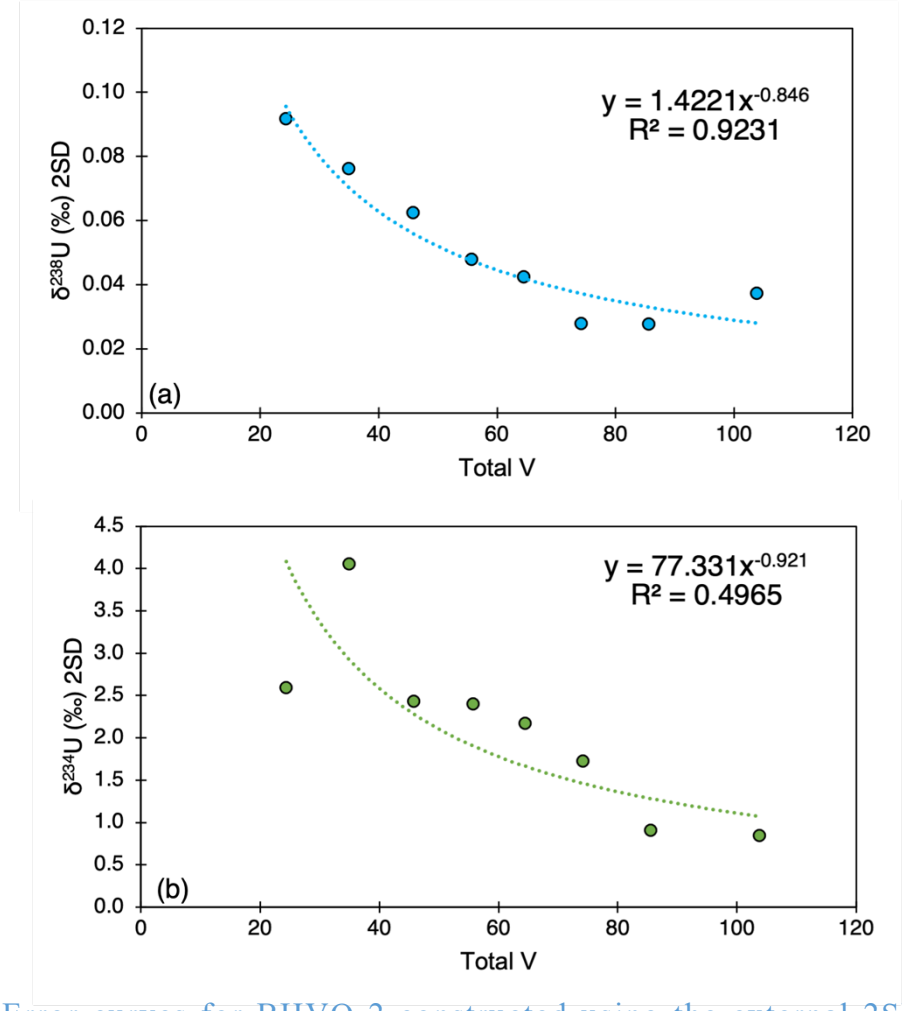

Fig. S2. Error curves for BHVO-2 constructed using the external 2SD of repeat measurements of BHVO-2 at various intensity brackets, 20 − 30 V, 30 − 40 V, 40 − 50 V, 50 − 60 V, 70 − 80 V and >80 V. A power law relationship is fit through the external 2SD. The relationship defined by the power law is then applied to approximate errors for unknown samples. (a) Error curve for $\delta^{238}U$ measurements, (b) Error curve for $\delta^{234}U$ measurements.

Sample	$\delta^{238}U$ (‰)	2SD	$\delta^{234}U$ (‰)	2SD	U (ng g^{-1})$^{+}$	N.M	N.S
BHVO-2	−0.306	0.04	−0.1	1.8	419	145	25
	−0.314	*0.02*	*0.9*	*2.4*	*386*	*16*	*8*
BCR-2	−0.255	0.04	0.6	1.4	1687	27	4
	−0.297	*0.02*	*1.1*	*1.0*	*1671*	*1*	*1*
BIR	−0.277	0.19	−5.1	8.6	8	6	3
	−0.285	*0.02*	*−0.6*	*1.0*	*8*	*1*	*1*
CZ1	−0.048	0.04	−0.2	1.8	7995	30	3
	−0.053	*0.03*	*0.1*	*2.7*		*15*	*2*
GUG11	−0.460	0.05	0.3	2.0	185	10	2
	−0.419	*0.03*	*−0.4*	*2.0*	*143*	*1*	*1*
IT3a	−0.289	0.06	0.1	2.6	70	26	10
	−0.296	*0.02*	*−0.3*	*1.7*	*62*	*3*	*1*
LP45d	−0.319	0.05	−0.2	2.0	2356	83	3
	−0.300	*0.02*	*−0.3*	*4.5*	*2119*	*5*	*2*
Uraninite	−0.548	0.05	−1.5	2.1	11985	51	3
W-2A	−0.291	0.04	2.0	1.4	497	37	7

Table S1. List of reference materials used to check reproducibility and precision during analytical sessions. Data in blue and italics are from Andersen et al. (2015). + Concentrations of U determined from isotope dilution. N.M is the number of individual measurements and N.S is the number of individual samples dissolved and processed through column chromatography.

Sample	BHVO-2	W-2A
Th (ng g^{-1})	1129	2112
Th 2SD	165	401
Th 2SE	14	51
U (ng g^{-1})	383	469
U 2SD	57	85
U 2SE	5	11
Th/U	2.9	4.5
N	147	63
Reference Th (ng g^{-1})	1114	2179
Reference U (ng g^{-1})	386	490
Reference Th/U	2.9	4.4

Table S2. List of reference materials used to check reproducibility and precision of measurements of Th and U concentrations measured on an Element2 ICP-MS. Reference values are from the USGS data sheets.

Section 3:

Ophiolite data and data tables

Sample	Lithology	$\delta^{238}U$ (‰)	2SE	$\delta^{234}U$ (‰)	2SE	U (ng g^{-1})	Th/U	N
Annieopsquotch 480 Ma								
VL01J188	SD	−0.297	0.052	35.4	2.2	34	6.3	3
VL01J189	SD	−0.324	0.049	28.7	2.0	21	4.3	2 (2)
VL01J190	SD	−0.267	0.048	18.7	2.0	97	4.6	2
VL01J191	SD	−0.306	0.023	34.2	0.9	137	4.3	3
VL01J192	SD	−0.498	0.064	25.9	2.7	22	4.7	2
VL01J193	SD	−0.287	0.055	32.5	2.3	19	5.9	2
VL01J194	SD	−0.344	0.052	34.3	2.2	35	4.8	2
VL01J195	Ex	−0.301	0.013	0.0	0.5	187	0.6	6 (2)
VL01J196a	Ex	−0.425	0.036	−9.5	1.5	66	1.7	4 (2)
VL01J196b	Ex	−0.267	0.021	5.3	0.9	49	4.2	4 (2)
VL01J198	Ex	−0.357	0.048	38.7	2.0	33	4.6	2
VL01J199a	Ex	−0.306	0.038	23.5	1.6	40	3.4	2
VL01J199b	Ex	−0.340	0.084	38.5	3.6	11	5.7	1
VL01J200a	Ex	−0.565	0.032	9.3	1.3	80	1.7	5 (2)
VL01J200b	Ex					6	10.0	
VL01J201	Ex	−0.484	0.049	25.3	2.1	61	3.6	3
VL01J202	Ex	−0.335	0.037	7.2	1.5	15	3.5	5 (2)
VL01J203	Ex	−0.300	0.050	23.7	2.1	39	3.2	2
VL01J204a	Ex	−0.399	0.022	11.6	0.9	128	1.4	8 (2)
VL01J204b	Ex	−0.409	0.032	14.5	1.3	76	2.7	5 (2)
VL01J205a	Ex	−0.528	0.027	12.6	1.1	48	2.5	3 (2)
VL01J205b	Ex	−0.356	0.027	−0.2	1.1	89	2.2	6 (2)
Khantaishir 540 Ma								
KT-11-24	G	−0.350	0.080	93.1	3.5	21	1.7	2
KT-11-149	G	−0.287	0.018	−29.1	0.7	164	2.9	2
KT-12-56	G	−0.254	0.057	51.7	2.4	28	2.1	2
KT-12-65	G					2	2.5	
KT-11-157	SD	−0.293	0.013	−28.7	0.5	336	3.3	5
KTB-4	SD	−0.201	0.016	1.5	0.6	154	0.8	5 (2)

KTU-4	SD	−0.471	0.040	4.0	1.7	23	3.1	5 (2)
KT-11-110	SD	−0.302	0.017	4.9	0.7	89	2.1	6 (2)
KT-11-83	SD	−0.522	0.028	18.2	1.1	120	0.7	2
KT-11-140	SD	−0.332	0.026	9.4	1.1	77	1.9	5 (2)
KTU-1	SD	−0.330	0.023	8.5	0.9	94	2.7	6 (2)
KT-12-78	SD	−0.321	0.027	21.7	1.1	77	2.0	2
KT-11-70	Ex	−0.399	0.019	442.2	0.7	183	0.6	2
KT-11-85	Ex	−0.496	0.058	183.6	2.4	35	2.1	1
KT-11-86	Ex	−0.238	0.027	38.4	1.1	115	0.7	2
KT-11-87	Ex	−0.590	0.047	61.9	2.0	40	2.5	2
KT-11-96	Ex	−0.338	0.019	9.7	0.7	115	1.6	5 (2)
KTP-1	Ex	−0.404	0.027	21.8	1.1	90	1.0	2
Gabal Gerf 750 Ma								
GG31	U					4	0.4	
GG35	U	−0.087	0.119	97.5	5.4	9	0.4	2
GG68	U	−0.400	0.075	1.5	3.2	19	0.0	2
GG74	U					3	0.2	
GG12	A	−0.261	0.029	26.0	1.2	88	4.4	2
GG257	A	−0.369	0.012	1.7	0.5	464	2.4	5
GG36	G					4	0.7	
GG77	G					10	3.2	
GG79	G	−0.241	0.067	18.7	2.9	16	2.7	2
GG80	G	−0.355	0.107	57.5	4.8	12	1.0	2
GG81	G	−0.199	0.046	9.2	2.0	85	2.8	3
GG82	G	−0.266	0.067	19.2	2.8	17	2.7	2
GG83	G					3	2.8	
GG84	G	−0.288	0.049	18.7	2.0	26	1.7	2
GG85	G	−0.199	0.052	32.0	2.2	25	1.3	2
GG86	G	−0.386	0.064	9.6	2.7	22	2.1	2
GG87	G					14	2.1	
GG88	G					5	3.4	
GG89	G					8	1.8	
GG90	G					8	2.9	
GG91	G					4	3.4	
GG92	G	−0.319	0.047	7.2	2.0	66	2.5	3
GG93	G					5	2.3	

GG71	SD	−0.287	0.022	16.5	0.9	42	2.6	2
GG72	SD	−0.275	0.018	24.9	0.7	44	3.6	2
GG95	SD					9	2.6	
GG170	SD					35	3.3	
GG171	SD					37	3.3	
GG172	SD	−0.208	0.038	40.0	1.5	20	2.0	2
GG173	SD					19	2.1	
GG174	SD	−0.208	0.028	23.9	1.1	39	2.1	2
GG175	SD					16	2.9	
GG176	SD					16	2.8	
GG177	SD					21	2.9	
GG281	SD	−0.244	0.034	7.1	1.4	36	1.8	2
GG9	Ex					87	3.3	
GG10	Ex	−0.250	0.026	1.8	1.0	42	3.1	2
GG13	Ex	−0.325	0.015	−12.4	0.6	304	4.6	3
GG69	Ex					50	3.8	
GG70	Ex					27	3.7	
GG73	Ex	−0.331	0.020	8.6	0.8	42	3.5	2
GG94	Ex					43	3.2	
GG178	Ex	−0.201	0.058	22.3	2.4	16	1.6	2
GG179	Ex	−0.719	0.034	9.3	1.4	22	1.2	2
GG180	Ex	−0.223	0.138	34.5	6.3	16	1.6	2
GG181	Ex					22	3.2	
GG182	Ex	−0.299	0.039	19.6	1.6	22	3.2	2
GG183	Ex					20	2.7	
GG184	Ex	−0.265	0.042	2.4	1.7	28	2.6	2
GG185	Ex					23	3.1	
GG282	Ex	−0.290	0.033	79.1	1.3	23	1.3	2

Table S3. Ophiolite U isotopic data, U concentration data and Th/U ratio data. For samples with measured U isotopic compositions the U concentrations have been calculated by isotope dilution. All Th concentration data and U concentration data for samples with no U isotopic data were acquired on an Element2 ICP-MS at the University of Bristol. N refers to the number of individual measurements and values in brackets the number of individual digestions and columns processed, 2SE is calculated from the method described in the Supplementary Material: Section 2. Lithology abbreviations: U = Ultramafic, A = Amphibolite, G = Gabbro, SD = Sheeted dyke, Ex = Extrusive section. Groupings have been made according to sample descriptions found in literature. In some cases, e.g., mainly for sheeted dykes, they can crosscut into other units; in these cases, the samples have been grouped still as part of the sheeted dykes. Samples highlighted in green are those that show clear signs of U enrichment (see main text for details).

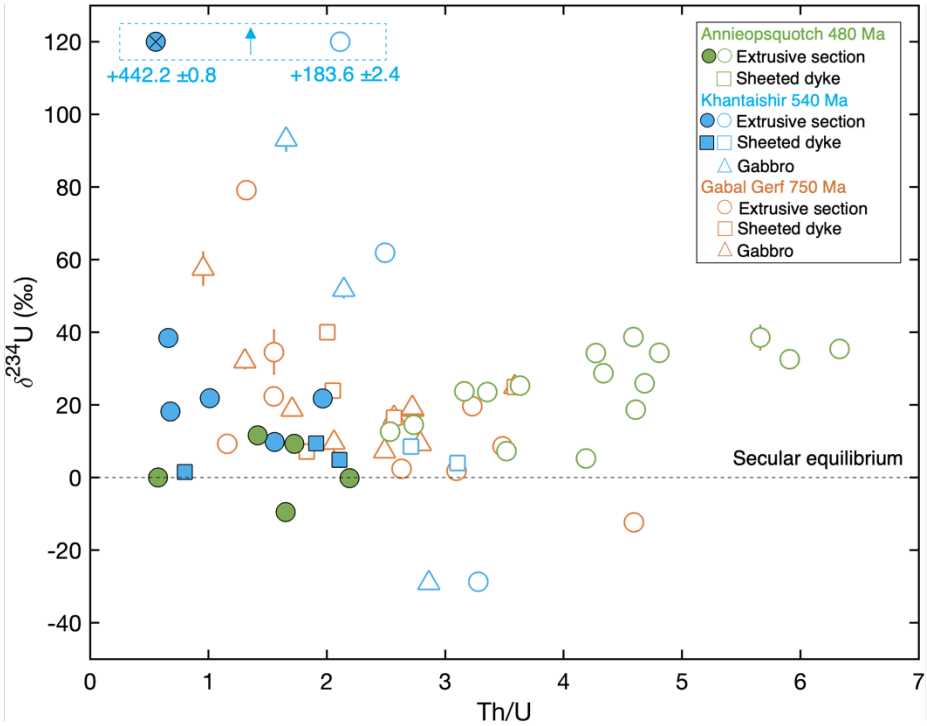

Fig. S3. (a) $\delta^{234}U$ vs. Th/U. Dashed black line at $\delta^{234}U = 0$ represents secular equilibrium. Samples from Khantaishir circled in the dashed blue box plot off the scale in $\delta^{234}U$ (Table S3). Error bars are 2SE.

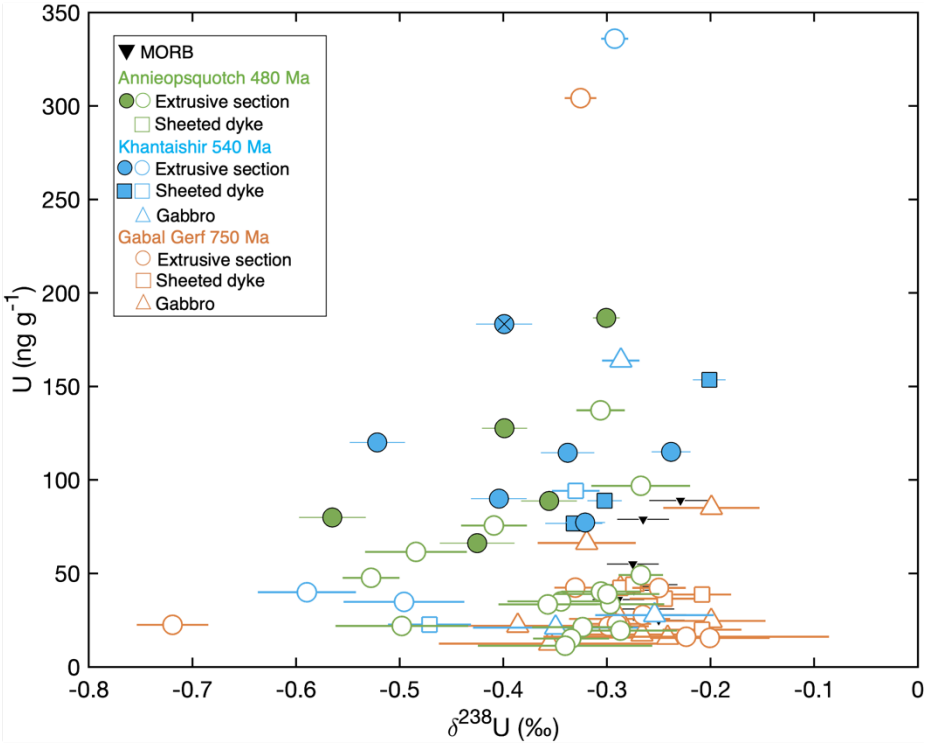

Fig. S4. Uranium concentration vs. $\delta^{238}U$. Samples of MORB (black inverted triangles) are from Andersen et al. (2015). Error bars are 2SE.

The main host minerals and sites for U in AMOC are poorly constrained, but current perspectives suggest that U uptake under oxic conditions in the shallow crust is associated with phases such as celadonite and Fe-oxyhydroxides, while under more reducing conditions in deeper portions of the crust uptake is associated with carbonates and in redox haloes (e.g., Staudigel et al., 1996; Bach et al., 2003; Kelley et al., 2005; Andersen et al., 2015, 2024).

Sample VL01J200b, a basalt from the Annieopsquotch ophiolite extrusive section, has only 6 ng g^{-1} U, reflecting either no U addition or U loss. The sample has a primary igneous ophitic texture, with laths of plagioclase encased by clinopyroxene, with some plagioclase altered to fine grained sericite (Fig. S5a). Sample VL01J200a, a pillow basalt from the same outcrop that shows clear U enrichment, shows alteration that is pervasive to light green to brown coloured secondary phyllosilicate minerals, such as micas, smectites and chlorites that overprint much of the primary igneous minerals and textures (Fig. S5b). This alteration is evident from brown saponite rims and turquoise green celadonite in rounded vesicles and interstitial areas. These alteration minerals are common in upper sections of AMOC (e.g., Alt et al., 2010 their figure 2), altered under oxidising conditions, also reflected in the low $\delta^{238}U$ composition (−0.565 ±0.032 ‰, 2SE) and a high U concentration (Table S3). Sample KTB4, a Khantaishir basaltic andesite from the sheeted dyke complex, has a fine-grained groundmass in which some primary clinopyroxene and plagioclase are preserved, while larger phenocrysts are replaced by phases such as calcite (Fig. S5c). This sample shows clear U enrichment and a U isotopic composition that is higher than some other extrusive samples and is similar to or just higher than modern MORB (−0.201 ±0.016 ‰, 2SE) (Fig. 2, table S3), potentially reflecting partial reduction and U uptake processes. A sample from a similar location in the sheeted dyke complex, KT-11-110, with a lower level of U enrichment has some minor secondary calcite and alteration to green coloured secondary minerals such as chlorite (Fig. S5d). This sample however has a $\delta^{238}U$ composition (−0.302 ±0.017 ‰, 2SE) similar to unaltered MORB in keeping with smaller amounts of U uptake and limited isotope fractionation, or quantitative U uptake. These observations reflect the heterogeneous nature of U addition to the oceanic crust during alteration, indicating similar alteration processes between Annieopsquotch, Khantaishir and modern AMOC (no thin sections were available for Gabel Gerf).

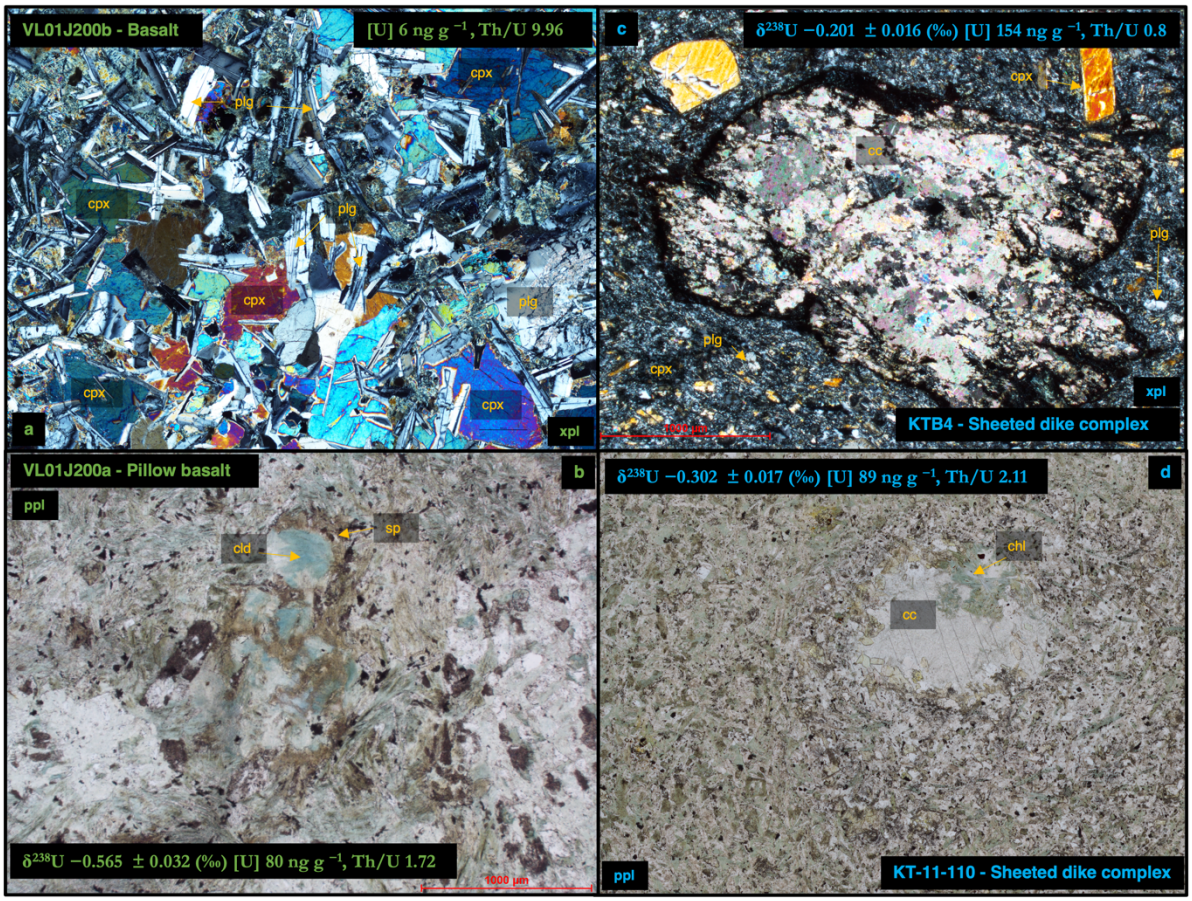

Fig. S5. Photomicrographs of ophiolite samples under plane polarised light (ppl) and cross polarised light (xpl). Scales are 1000 µm and are denoted by red lines on (b) and (c), the same scales apply to (a) and (d). Mineral abbreviations are, plg – Plagioclase feldspar, cpx – Clinopyroxene, cc – Calcite, cld – Celadonite, sp – Saponite, chl – Chlorite. (a) Primary igneous textures, with little signs of alteration, no U addition, and potential U loss. (b) Oxic alteration style with green coloured minerals in ppl, with U addition under oxic conditions giving rise to low Th/U and low $\delta^{238}U$. (c) Large pyroxene phenocryst replaced to calcite, reflecting more reducing conditions with high U uptake giving rise to low Th/U and high $\delta^{238}U$. (d) Lower degrees of visible alteration that is also reflected in more muted U uptake and muted U isotopic fractionation.

Section 4:

Recent U addition from a groundwater source modelling

We can estimate the potential impact of recent sub-aerial U uptake on $\delta^{238}U$ compositions by assuming that the $\delta^{234}U$ compositions of samples with $\delta^{234}U > 0$ is a mixture between recent U uptake from a groundwater fluid with an assumed high $\delta^{234}U$ and older (>2 Ma) U with $\delta^{234}U = 0$. We take the approach of Andersen et al. (2024) and assume a $\delta^{234}U$ for the fluid adding U of +1000 ‰ (Osmond and Cowart, 1976). Using this mixture between recent added U and older U we calculate the fraction of U in samples that was added recently (Table S4). This estimate shows generally low amounts of recently added U (<10 %), but for some samples in Khantaishir ranges up to ~ 44 %. Removing this recent added U from samples results in minimal change in Th/U ratios of most samples (Fig. S6a), especially those with $\delta^{234}U$ closest to secular equilibrium and the most enriched in U, with the largest change in sample KT-11-70 ($\delta^{234}U$ = +442 ‰). We also apply the same correction to $\delta^{238}U$ values by assuming the fluid adding recent U has a $\delta^{238}U$ compositions of the highest and lowest $\delta^{238}U$ composition in each ophiolite. Again, most samples show minimal change in $\delta^{238}U$ (<0.1 ‰) and are generally within analytical uncertainty (Fig. S6b & c), especially for samples that show the most U enrichment. This is however bar sample KT-11-70 (marked with a x on figures 2, 3, S3, S4, and S6) which shows the largest change outside of uncertainty.

Sample	Lithology	$\delta^{238}U$ (‰)	$\delta^{234}U$ (‰)	U (ng g^{-1})	Th/U	Fraction U added	Added U (ng g^{-1})	Th/U Corrected	$\delta^{238}U$ (‰) Corrected[a]	$\delta^{238}U$ (‰) Corrected[b]
Annieopsquotch 480 Ma										
VL01J188	SD	−0.297	35.4	34	6.3	0.04	1.2	6.6	−0.287	−0.298
VL01J189	SD	−0.324	28.7	21	4.3	0.03	0.6	4.5	−0.316	−0.325
VL01J190	SD	−0.267	18.7	97	4.6	0.02	1.8	4.7	−0.262	−0.267
VL01J191	SD	−0.306	34.2	137	4.3	0.03	4.7	4.4	−0.297	−0.307
VL01J192	SD	−0.498	25.9	22	4.7	0.03	0.6	4.8	−0.496	−0.504
VL01J193	SD	−0.287	32.5	19	5.9	0.03	0.6	6.1	−0.278	−0.288
VL01J194	SD	−0.344	34.3	35	4.8	0.03	1.2	5.0	−0.336	−0.347
VL01J195	Ex	−0.301	0.0	187	0.6	0.00	0.0	0.6	−0.301	−0.301
VL01J196a	Ex	−0.425	−9.5	66	1.7					
VL01J196b	Ex	−0.267	5.3	49	4.2	0.01	0.3	4.2	−0.266	−0.267
VL01J198	Ex	−0.357	38.7	33	4.6	0.04	1.3	4.8	−0.349	−0.361
VL01J199a	Ex	−0.306	23.5	40	3.4	0.02	0.9	3.4	−0.300	−0.307
VL01J199b	Ex	−0.340	38.5	11	5.7	0.04	0.4	5.9	−0.331	−0.343
VL01J200a	Ex	−0.565	9.3	80	1.7	0.01	0.7	1.7	−0.565	−0.568
VL01J200b	Ex			6	10.0					
VL01J201	Ex	−0.484	25.3	61	3.6	0.03	1.6	3.7	−0.482	−0.490
VL01J202	Ex	−0.335	7.2	15	3.5	0.01	0.1	3.5	−0.333	−0.335
VL01J203	Ex	−0.300	23.7	39	3.2	0.02	0.9	3.2	−0.293	−0.300
VL01J204a	Ex	−0.399	11.6	128	1.4	0.01	1.5	1.4	−0.397	−0.400
VL01J204b	Ex	−0.409	14.5	76	2.7	0.01	1.1	2.8	−0.407	−0.411
VL01J205a	Ex	−0.528	12.6	48	2.5	0.01	0.6	2.6	−0.527	−0.531
VL01J205b	Ex	−0.356	−0.2	89	2.2					
Khantaishir 540 Ma										
KT-11-24	G	−0.350	93.1	21	1.7	0.09	2.0	1.8	−0.325	−0.365
KT-11-149	G	−0.287	−29.1	164	2.9					
KT-12-56	G	−0.254	51.7	28	2.1	0.05	1.4	2.3	−0.236	−0.257
KT-12-65	G			2	2.5					
KT-11-157	SD	−0.293	−28.7	336	3.3					
KTB-4	SD	−0.201	1.5	154	0.8	0.00	0.2	0.8	−0.201	−0.201
KTU-4	SD	−0.471	4.0	23	3.1	0.00	0.1	3.1	−0.471	−0.472
KT-11-110	SD	−0.302	4.9	89	2.1	0.00	0.4	2.1	−0.301	−0.303
KT-11-83	SD	−0.522	18.2	120	0.7	0.02	2.2	0.7	−0.520	−0.527
KT-11-140	SD	−0.332	9.4	77	1.9	0.01	0.7	1.9	−0.330	−0.333
KTU-1	SD	−0.330	8.5	94	2.7	0.01	0.8	2.7	−0.328	−0.331
KT-12-78	SD	−0.321	21.7	77	2.0	0.02	1.7	2.0	−0.315	−0.324
KT-11-70	Ex	−0.399	442.2	183	0.6	0.44	81.1	1.0	−0.248	−0.556
KT-11-85	Ex	−0.496	183.6	35	2.1	0.18	6.4	2.6	−0.475	−0.562
KT-11-86	Ex	−0.238	38.4	115	0.7	0.04	4.4	0.7	−0.224	−0.240
KT-11-87	Ex	−0.590	61.9	40	2.5	0.06	2.5	2.7	−0.590	−0.615
KT-11-96	Ex	−0.338	9.7	115	1.6	0.01	1.1	1.6	−0.335	−0.339
KTP-1	Ex	−0.404	21.8	90	1.0	0.02	2.0	1.0	−0.400	−0.409
Gabal Gerf 750 Ma										
GG31	U			4	0.4					
GG35	U	−0.087	97.5	9	0.4					
GG68	U	−0.400	1.5	19	0.0					
GG74	U			3	0.2					
GG12	A	−0.261	26.0	88	4.4					
GG257	A	−0.369	1.7	464	2.4					
GG36	G			4	0.7					
GG77	G			10	3.2					
GG79	G	−0.241	18.7	16	2.7	0.02	0.3	2.8	−0.232	−0.242
GG80	G	−0.355	57.5	12	1.0	0.06	0.7	1.0	−0.333	−0.365
GG81	G	−0.199	9.2	85	2.8	0.01	0.8	2.8	−0.194	−0.199
GG82	G	−0.266	19.2	17	2.7	0.02	0.3	2.8	−0.257	−0.267

GG83	G			3	2.8					
GG84	G	−0.288	18.7	26	1.7	0.02	0.5	1.7	−0.279	−0.289
GG85	G	−0.199	32.0	25	1.3	0.03	0.8	1.3	−0.182	−0.199
GG86	G	−0.386	9.6	22	2.1	0.01	0.2	2.1	−0.383	−0.388
GG87	G			14	2.1					
GG88	G			5	3.4					
GG89	G			8	1.8					
GG90	G			8	2.9					
GG91	G			4	3.4					
GG92	G	−0.319	7.2	66	2.5	0.01	0.5	2.5	−0.317	−0.320
GG93	G			5	2.3					
GG71	SD	−0.287	16.5	42	2.6	0.02	0.7	2.6	−0.280	−0.288
GG72	SD	−0.275	24.9	44	3.6	0.02	1.1	3.7	−0.263	−0.277
GG95	SD			9	2.6					
GG170	SD			35	3.3					
GG171	SD			37	3.3					
GG172	SD	−0.208	40.0	20	2.0	0.04	0.8	2.1	−0.187	−0.209
GG173	SD			19	2.1					
GG174	SD	−0.208	23.9	39	2.1	0.02	0.9	2.1	−0.196	−0.208
GG175	SD			16	2.9					
GG176	SD			16	2.8					
GG177	SD			21	2.9					
GG281	SD	−0.244	7.1	36	1.8	0.01	0.3	1.8	−0.241	−0.245
GG9	Ex			87	3.3					
GG10	Ex	−0.250	1.8	42	3.1	0.00	0.1	3.1	−0.249	−0.250
GG13	Ex	−0.325	−12.4	304	4.6					
GG69	Ex			50	3.8					
GG70	Ex			27	3.7					
GG73	Ex	−0.331	8.6	42	3.5	0.01	0.4	3.5	−0.327	−0.332
GG94	Ex			43	3.2					
GG178	Ex	−0.201	22.3	16	1.6	0.02	0.3	1.6	−0.189	−0.201
GG179	Ex	−0.719	9.3	22	1.2	0.01	0.2	1.2	−0.719	−0.724
GG180	Ex	−0.223	34.5	16	1.6	0.03	0.6	1.6	−0.206	−0.224
GG181	Ex			22	3.2					
GG182	Ex	−0.299	19.6	22	3.2	0.02	0.4	3.3	−0.290	−0.300
GG183	Ex			20	2.7					
GG184	Ex	−0.265	2.4	28	2.6	0.00	0.1	2.6	−0.264	−0.265
GG185	Ex			23	3.1					
GG282	Ex	−0.290	79.1	23	1.3	0.08	1.8	1.4	−0.254	−0.298

Table S4. Ophiolite samples corrected for a recent flux of groundwater U addition, using an estimated groundwater composition of $\delta^{234}U$ = 1000 ‰. Readers are referred to the online version of the supplementary data tables for calculations. a – Samples corrected in $\delta^{238}U$ using lowest $\delta^{238}U$ in each ophiolite, b – Samples corrected in $\delta^{238}U$ using highest $\delta^{238}U$ in each ophiolite.

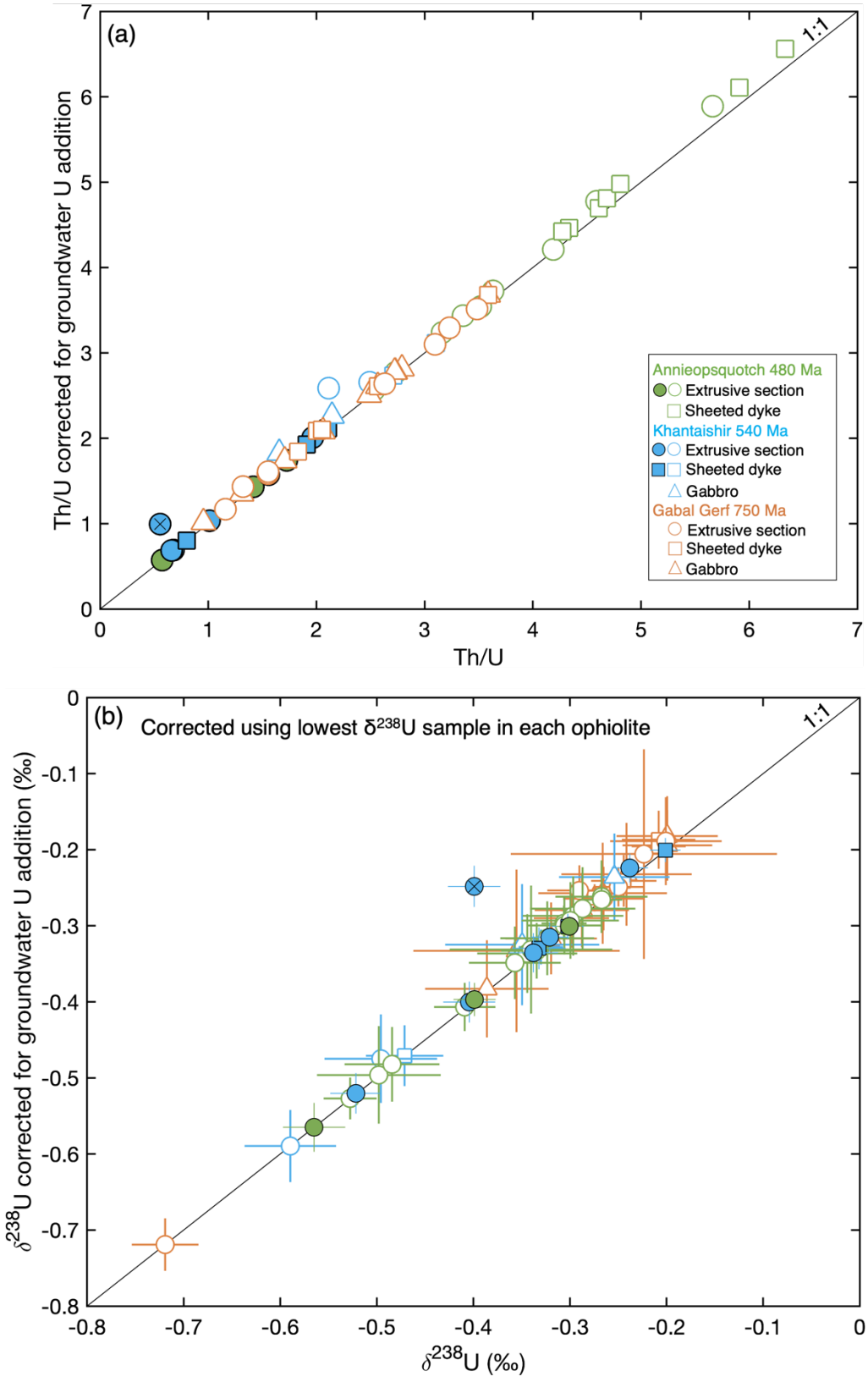
(a)
1:1
Th/U corrected for groundwater U addition
Th/U
Annieopsquotch 480 Ma
Extrusive section
Sheeted dyke
Khantaishir 540 Ma
Extrusive section
Sheeted dyke
Gabbro
Gabal Gerf 750 Ma
Extrusive section
Sheeted dyke
Gabbro
(b)
Corrected using lowest δ238U sample in each ophiolite
1:1
δ238U corrected for groundwater U addition (‰)
δ238U (‰)

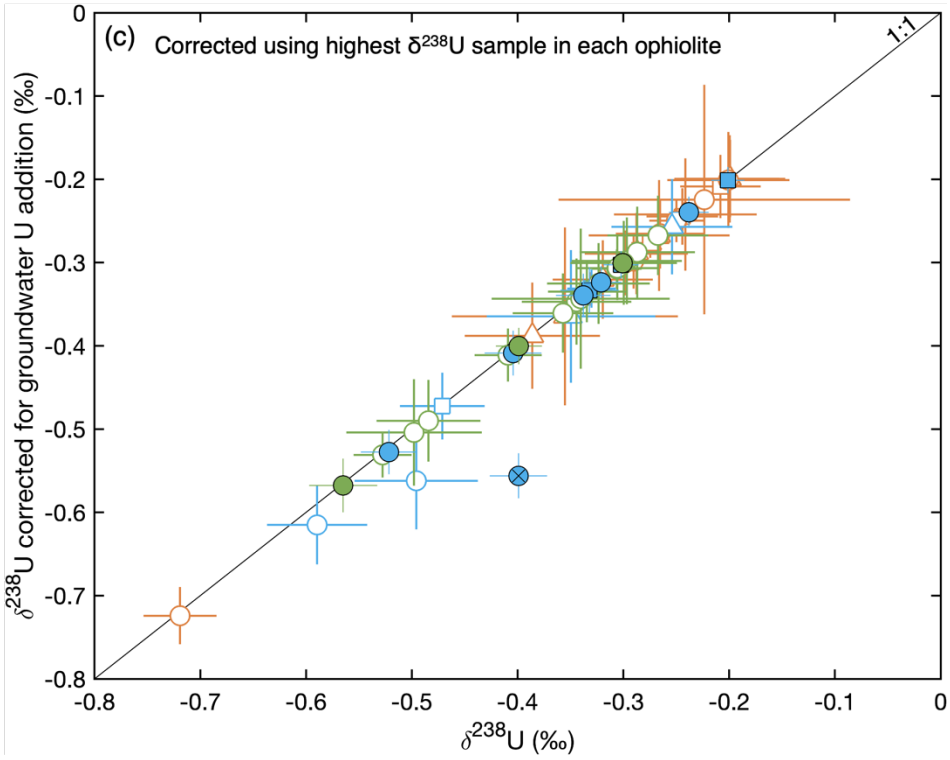

Fig. S6. (a) Th/U and (b & c) $\delta^{238}U$ composition of ophiolite samples corrected for recent U addition from a groundwater source versus measured compositions, see Supplementary Material Section: 4 for details of modelling. The black diagonal line represents the 1:1 line. In (b) data are corrected using the lowest $\delta^{238}U$ composition in each respective ophiolite and in (c) the highest $\delta^{238}U$ composition. Error bars are 2SE.

Section 5:

Uranium enrichment and isotopic variation in AMOC calculations

Altered mafic oceanic crust	Age (Ma)	Region	DIB (m)	Spreading type	U MORB (ng g^{-1})	U AMOC (ng g^{-1})	Relative U enrichment	$\delta^{238}U$ (‰)	2SE
1256D mean of sections[a]	15	Pacific	1250	Fast	50	116	2.3	−0.518	0.213
1256D all[a]						93	1.9	−0.375	0.059
417/418[b]	120	Atlantic	550	Slow	35	321	9.2	−0.200	0.222
801B/C	167	W. Pacific	400	Fast	44	390	8.9	−0.232	0.158
801C - Supercomposite[c]								−0.170	0.026
Ophiolite									
Annieopsquotch enriched[d]	480				43*	110	2.6	−0.386	0.089
Annieopsquotch all						61	1.4	−0.364	0.038
Khantaishir enriched[d]	540				43*	113	2.6	−0.285	0.071
Khantaishir all						103	2.4	−0.334	0.052
Gabal Gerf	750				43*	44	1.0	−0.294	0.047

Table S5. Altered mafic oceanic crust and ophiolite data used to produce figure 4. DIB: Depth in basement, is the length of oceanic crust drill core recovered. Relative U enrichment is calculated as U concentration in AMOC / U concentration in MORB. Isotopic U composition, $\delta^{238}U$, is calculated as a U concentration weighted average, and the 2SE from the 2SD across samples and sections averaged. Data is compiled from the following sources, a: 1256D compiled data and U isotopic data from Andersen et al. (2024), where the U concentration of MORB is the average of fresh East Pacific Rise MORB glass data from Andersen et al. (2015) and U concentration of AMOC is the average of data from Harris (2011). The mean of sections is the average of all sections excluding the plutonic section and 'all' is the average of all discrete samples measured. b: 417/418 Fresh MORB and AMOC (represented by a supercomposite sample) is from Staudigel et al. (1995, 1996) and Kelley et al. (2005) (supercomposite). U isotopic data is from Noordmann et al. (2016). c: 801 Fresh MORB and AMOC (represented by a supercomposite sample) is from Kelley et al. (2003, 2005); U isotopic data is from Andersen et al. (2015) and Noordmann et al. (2016), U isotopic data for 801C is split into a U concentration weighted average for altered non-composite samples and a measurement of the supercomposite. d: Average data for ophiolite samples that show clear U enrichment (see main text for details). *Ophiolite sample enrichment average is calculated from the average U concentration of all samples (excluding peridotite and amphibolite) or those showing clear U enrichment (see main text for details) relative to an average value for fresh MORB from the ocean drill sites (~ 43 ng g^{-1}).

Section 6:

Iron systematics

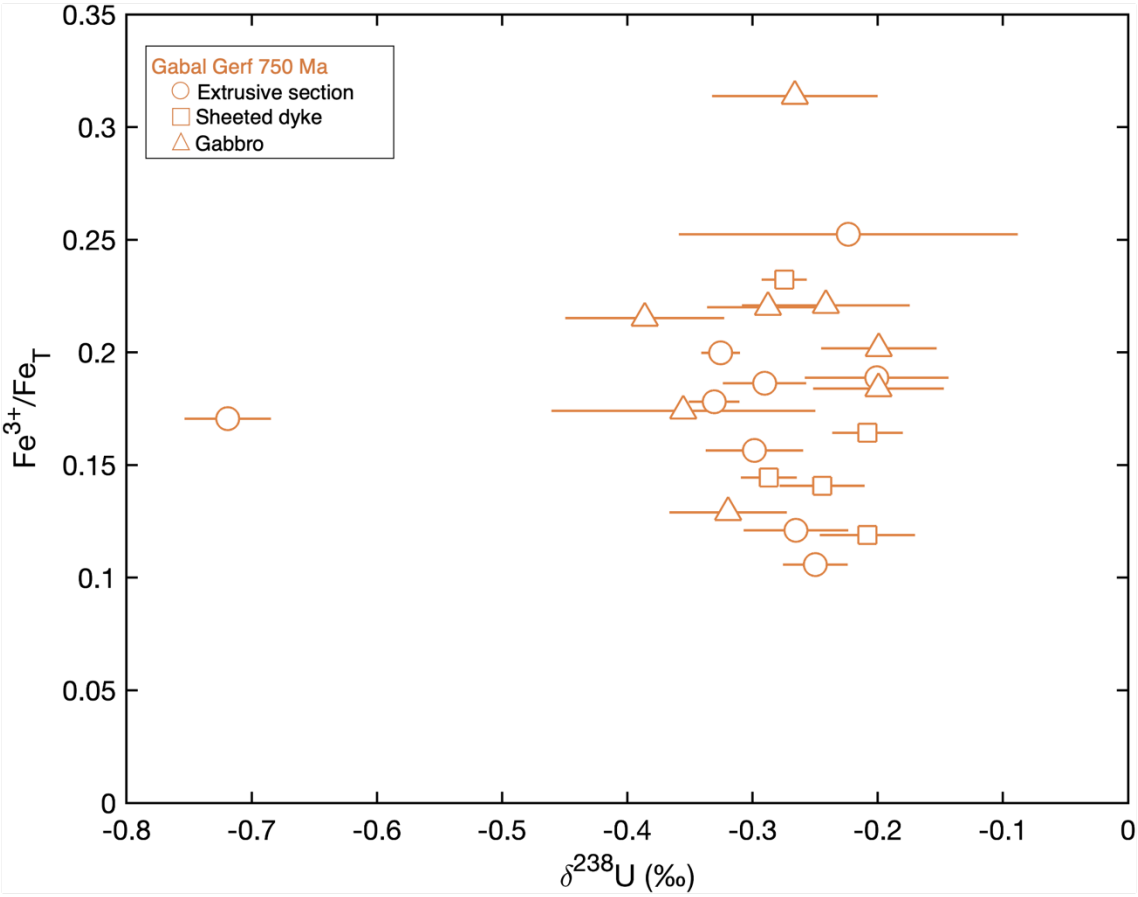

Fig. S7. Variation in Fe^{3+}/Fe_T vs. $\delta^{238}U$ for Gabal Gerf samples. Iron data is from Zimmer et al. (1995). Error bars are 2SE.

References

Alt, J. C., C. Laverne, R. M. Coggon, D. A. H. Teagle, N. R. Banerjee, S. Morgan, C. E. Smith-Duque, M. Harris, and L. Galli, 2010, Subsurface structure of a submarine hydrothermal system in ocean crust formed at the East Pacific Rise, ODP/IODP Site 1256: Submarine hydrothermal system: Geochemistry, Geophysics, Geosystems, **11**, Q10010.

Andersen, M. B., S. Romaniello, D. Vance, S. H. Little, R. Herdman, and T. W. Lyons, 2014, A modern framework for the interpretation of $^{238}U/^{235}U$ in studies of ancient ocean redox: Earth and Planetary Science Letters, **400**, 184–194.

Andersen, M. B., T. Elliott, H. Freymuth, K. W. W. Sims, Y. Niu, and K. A. Kelley, 2015, The terrestrial uranium isotope cycle: Nature, **517**, 356–359.

Andersen, M. B., J. B. Rodney, H. Freymuth, F. Vils, M. Harris, K. Cooper, D. A. H. Teagle, and T. Elliott, 2024, Time scales and mechanisms of uranium uptake in altered ocean crust; observations from the ~15 million year-old site 1256 in the eastern equatorial Pacific: Geochimica et Cosmochimica Acta, **382**, 142–159.

Bach, W., B. Peucker-Ehrenbrink, S. R. Hart, and J. S. Blusztajn, 2003, Geochemistry of hydrothermally altered oceanic crust: DSDP/ODP Hole 504B - Implications for seawater-crust exchange budgets and Sr- and Pb-isotopic evolution of the mantle: Hydrothermally altered oceanic crust: Geochemistry, Geophysics, Geosystems, **4**, 8904.

Cheng, H., R. Lawrence Edwards, C.-C. Shen, V. J. Polyak, Y. Asmerom, J. Woodhead, J. Hellstrom, Y. Wang, X. Kong, C. Spötl, X. Wang, and E. Calvin Alexander, 2013, Improvements in ^{230}Th dating, ^{230}Th and ^{234}U half-life values, and U–Th isotopic measurements by multi-collector inductively coupled plasma mass spectrometry: Earth and Planetary Science Letters, **371–372**, 82–91.

Condon, D. J., N. McLean, S. R. Noble, and S. A. Bowring, 2010, Isotopic composition ($^{238}U/^{235}U$) of some commonly used uranium reference materials: Geochimica et Cosmochimica Acta, **74**, 7127–7143.

Dilek, Y., and H. Furnes, 2011, Ophiolite genesis and global tectonics: Geochemical and tectonic fingerprinting of ancient oceanic lithosphere: Geological Society of America Bulletin, **123**, 387–411.

Gale, A., C. A. Dalton, C. H. Langmuir, Y. Su, and J.-G. Schilling, 2013, The mean composition of ocean ridge basalts: Geochemistry, Geophysics, Geosystems, **14**, 489–518.

1827 Gianola, O., M. W. Schmidt, O. Jagoutz, J. Rickli, O. Bruguier, and O. Sambuu, 2019, The Crust–
1828 Mantle Transition of the Khantaishir Arc Ophiolite (Western Mongolia): Journal of
1829 Petrology, **60**, 673–700.
1830 Harris, M., 2011, The Accretion of Lower Oceanic Crust. PhD thesis University of Southampton.
1831 Hiess, J., D. J. Condon, N. McLean, and S. R. Noble, 2012, $^{238}U/^{235}U$ Systematics in Terrestrial
1832 Uranium-Bearing Minerals: Science, **335**, 1610–1614.
1833 Kelley, K., T. Plank, L. Farr, J. Ludden, and H. Staudigel, 2005, Subduction cycling of U, Th, and
1834 Pb: Earth and Planetary Science Letters, **234**, 369–383.
1835 Kelley, K. A., T. Plank, J. Ludden, and H. Staudigel, 2003, Composition of altered oceanic crust
1836 at ODP Sites 801 and 1149: Geochemistry, Geophysics, Geosystems, **4**, 8910.
1837 Lissenberg, C. J., C. R. van Staal, J. H. Bédard, and A. Zagorevski, 2005, Geochemical constraints
1838 on the origin of the Annieopsquotch ophiolite belt, Newfoundland Appalachians:
1839 Geological Society of America Bulletin, **117**, 1413.
1840 Noordmann, J., S. Weyer, R. B. Georg, S. Jöns, and M. Sharma, 2016, $^{(238)}U/^{(235)}U$ isotope ratios of
1841 crustal material, rivers and products of hydrothermal alteration: new insights on the
1842 oceanic U isotope mass balance: Isotopes in Environmental and Health Studies, **52**, 141–
1843 163.
1844 Osmond, J. K., and J. B. Cowart, 1976, The theory and uses of natural uranium isotopic variations
1845 in hydrology: Atomic Energy Review, **14**, 621–679.
1846 Richter, S., A. Alonso-Munoz, R. Eykens, U. Jacobsson, H. Kuehn, A. Verbruggen, Y. Aregbe, R.
1847 Wellum, and E. Keegan, 2008, The isotopic composition of natural uranium samples -
1848 Measurements using the new $n(^{233}U)/n(^{236}U)$ double spike IRMM-3636: International
1849 Journal of Mass Spectrometry, **269**, 145–148.
1850 Staudigel, H., T. Plank, B. White, and H.-U. Schmincke, 1996, Geochemical Fluxes During
1851 Seafloor Alteration of the Basaltic Upper Oceanic Crust: DSDP Sites 417 and 418, *in*
1852 Subduction, eds: G.E Bebout, D.W. Scholl, S.H. Kirby and J.P. Platt), Geophysical
1853 Monograph Series, 96, American Geophysical Union (AGU), 19–38.
1854 Staudigel, H., G. R. Davies, S. R. Hart, K. M. Marchant, and Brian. M. Smith, 1995, Large scale
1855 isotopic Sr, Nd and O isotopic anatomy of altered oceanic crust: DSDP/ODP sites
1856 417/418: Earth and Planetary Science Letters, **130**, 169–185.
1857 Zimmer, M., A. Kröner, K. P. Jochum, T. Reischmann, and W. Todt, 1995, The Gabal Gerf
1858 complex: A precambrian N-MORB ophiolite in the Nubian Shield, NE Africa: Chemical
1859 Geology, **123**, 29–51.
1860

1861